Origin of Dawnside Subauroral Polarization Streams during Major Geomagnetic Storms

Dong Lin[1], Wenbin Wang[2], Viacheslav G. Merkin[3], Chaosong Huang[4], Meers M. Oppenheim[5], Kareem Sorathia[3], Kevin H Pham[1], Adam Michael[6], Shanshan Bao[7], Qian Wu[8], Yongliang Zhang[3], Michael Wiltberger[8], Frank R. Toffoletto[7], John Lyon[9], and Jeffrey Garretson[10]

[1]National Center for Atmospheric Research
[2]HAO/NCAR
[3]The Johns Hopkins University Applied Physics Laboratory
[4]Air Force Research Laboratory
[5]Boston University
[6]The John Hopkins Applied Physics Laboratory
[7]Rice University
[8]National Center for Atmospheric Research (UCAR)
[9]Dartmouth College
[10]Johns Hopkins Applied Physics Lab

November 28, 2022

Abstract

Solar eruptions cause geomagnetic storms in the near-Earth environment, creating spectacular aurorae visible to the human eye and invisible dynamic changes permeating all of geospace. Just equatorward of the aurora, radars and satellites often observe intense westward plasma flows called subauroral polarization streams (SAPS) in the dusk-to-midnight ionosphere. SAPS occur across a narrow latitudinal range and lead to intense frictional heating of the ionospheric plasma and atmospheric neutral gas. SAPS also generate small-scale plasma waves and density irregularities that interfere with radio communications. As opposed to the commonly observed duskside SAPS, intense eastward subauroral plasma flows in the morning sector were recently discovered to have occurred during a super storm on 20 November 2003. However, the origin of these flows termed "dawnside SAPS" could not be explained by the same mechanism that causes SAPS on the duskside and has remained a mystery. Through real-event global geospace simulations, here we demonstrate that dawnside SAPS can only occur during major storm conditions. During these times the magnetospheric plasma convection is so strong as to effectively transport ions to the dawnside, whereas they are typically deflected to the dusk by the energy-dependent drifts. Ring current pressure then builds up on the dawnside and drives field-aligned currents that connect to the subauroral ionosphere, where eastward SAPS are generated. The origin of dawnside SAPS explicated in this study advances our understanding of how the geospace system responds to strongly disturbed solar wind driving conditions that can have severe detrimental impacts on human society and infrastructure.

Origin of Dawnside Subauroral Polarization Streams during Major Geomagnetic Storms

Dong Lin[1], Wenbin Wang[1], Viacheslav Merkin[2], Chaosong Huang[3], Meers Oppenheim[4], Kareem Sorathia[2], Kevin Pham[1], Adam Michael[2], Shanshan Bao[5], Qian Wu[1], Yongliang Zhang[2], Michael Wiltberger[1], Frank Toffoletto[5], John Lyon[6], and Jeffrey Garretson[2]

[1]High Altitude Observatory, National Center for Atmospheric Research, Boulder, CO
[2]Applied Physics Laboratory, Johns Hopkins University, Laurel, MD
[3]Space Vehicles Directorate, Air Force Research Laboratory, Kirtland AFB, NM
[4]Astronomy Department, Boston University, Boston, MA
[5]Department of Physics and Astronomy, Rice University, Houston, TX
[6]Department of Physics and Astronomy, Dartmouth College, Hanover, NH

Key Points:

- Dawnside SAPS occur during the main and recovery phases of major geomagnetic storms.
- Strong magnetospheric convection transports energetic ions to the dawnside and inner magnetosphere during major storms.
- Substantial subauroral upward field-aligned currents develop on the dawnside to drive the eastward SAPS.

Corresponding author: Dong Lin, `ldong@ucar.edu`

Abstract

Solar eruptions cause geomagnetic storms in the near-Earth environment, creating spectacular aurorae visible to the human eye and invisible dynamic changes permeating all of geospace. Just equatorward of the aurora, radars and satellites often observe intense westward plasma flows called subauroral polarization streams (SAPS) in the dusk-to-midnight ionosphere. SAPS occur across a narrow latitudinal range and lead to intense frictional heating of the ionospheric plasma and atmospheric neutral gas. SAPS also generate small-scale plasma waves and density irregularities that interfere with radio communications. As opposed to the commonly observed duskside SAPS, intense eastward subauroral plasma flows in the morning sector were recently discovered to have occurred during a super storm on 20 November 2003. However, the origin of these flows termed "dawnside SAPS" could not be explained by the same mechanism that causes SAPS on the duskside and has remained a mystery. Through real-event global geospace simulations, here we demonstrate that dawnside SAPS can only occur during major storm conditions. During these times the magnetospheric plasma convection is so strong as to effectively transport ions to the dawnside, whereas they are typically deflected to the dusk by the energy-dependent drifts. Ring current pressure then builds up on the dawnside and drives field-aligned currents that connect to the subauroral ionosphere, where eastward SAPS are generated. The origin of dawnside SAPS explicated in this study advances our understanding of how the geospace system responds to strongly disturbed solar wind driving conditions that can have severe detrimental impacts on human society and infrastructure.

Plain Language Summary

Solar eruptions of mass and magnetic field can trigger geospace storms. The most well-known storm phenomenon is the aurorae in the Earth's high latitude upper atmosphere. Below the latitude of auroral boundary, i.e., in the subauroral region, westward plasma flows from hundreds of m/s to a few km/s are often observed from afternoon to midnight during geomagnetically active periods. The fast plasma flows have important space weather effects due to their very large speed over a narrow latitudinal range. It was newly discovered that similar fast eastward plasma flows exist on the dawnside subauroral region during an extreme geomagnetic storm on 20 November 2003. However, origin of the dawnside subauroral fast flow is still a mystery. This study demonstrates that the dawnside subauroral fast flow only occurs during very strong geomagnetic storms when the magnetospheric ions can be transported to and accumulate in the morning sector to build up plasma pressure and currents to generate the subauroral plasma flow in the ionosphere. This mechanism is important for us to understand how the geospace responds to geomagnetic storms, especially when the storm activity level is extremely high that it may have severe adverse effects on human society and infrastructure.

1 Introduction

Aurorae are the most prominent visible manifestations of geomagnetic storms caused by solar disturbances. Just equatorward of the aurora, invisible to the human eye, radars and orbiting satellites often observe in the dusk-to-midnight ionosphere intense westward plasma flows with speeds from hundreds of m/s to a few km/s, called subauroral polarization streams (SAPS). SAPS have important space weather effects due to the very large plasma flow velocity variation across a narrow latitudinal range of typically less than $\sim 5°$ (e.g., Foster et al., 2002). This mesoscale structure of SAPS can result in locally enhanced thermospheric temperature (e.g., Wang et al., 2012), small-scale electric field oscillations (e.g., Foster et al., 2004), and plasma density irregularities (e.g., Mishin & Blaunstein, 2008). Various data sources have revealed that SAPS occur mostly in the dusk sector although the westward SAPS flow channel may extend to the post-midnight and early morning sectors during strong geomagnetic activity (e.g., Foster et al., 2002; He et al., 2014; Kunduri et al., 2017; Landry & Anderson, 2018; Aa et al., 2020). The preponderance of SAPS on the duskside is explained by the physics of their generation. SAPS are driven by a strong poleward electric field equatorward of the electron auroral boundary where the ionospheric conductance is relatively low but there are still finite downward field-aligned currents (FACs) in the low latitude portion of the Region-2 FACs (e.g., P. Anderson et al., 1993, 2001; Foster et al., 2002; Mishin et al., 2017). The gap between the equatorward boundaries of electron precipitation and downward Region-2 FACs originates from the inner magnetosphere. During geomagnetically active times, ions penetrate deeper and closer to the Earth than electrons, making the ion ring current inner boundary more inward than the electron plasma sheet (e.g., Califf et al., 2016). However, since the ion magnetic drifts are westward, the ring current pressure peak is usually located in the premidnight sector (e.g., Fok et al., 1996). The Region-2 FACs, which are mainly driven by the azimuthal gradient of ring current pressure (e.g., Vasyliunas, 1970), also tend to shift further equatorward and be more intense on the duskside than on the dawnside (e.g., Ebihara & Ejiri, 2000; B. Anderson et al., 2005; Zheng et al., 2006). On the other hand, electrons drift eastward making the diffuse electron precipitation centered in the postmidnight sector. The equatorward precipitation boundary is located at a lower latitude on the dawnside than on the duskside (e.g., Newell et al., 2009). Deeper penetration of ions than electrons thus occurs more often in the dusk to midnight sector. It is, therefore, not surprising that SAPS occur predominantly on the duskside and flow westward.

However, Horvath and Lovell (2021) and Huang et al. (2021) recently reported eastward plasma flows in the dawnside subauroral region observed by the Defense Meteorology Satellite Programs (DMSP) satellites during the 20 November 2003 super storm, which they termed "dawnside SAPS". Here, as a convention, a geomagnetic storm is classified by its minimum disturbance storm time index Dst_{min} (e.g., Gonzalez et al., 1994; J. Zhang et al., 2003). A storm is designated as weak if -50 nT$< Dst_{min} <$ -30 nT, moderate if -100 nT $< Dst_{min} <$ -50 nT, intense if -250 nT $< Dst_{min} <$ -100 nT, or a superstorm if $Dst_{min} <$ -250 nT. Furthermore, we refer to intense and super storms together as major storms. Similar to the duskside SAPS, dawnside SAPS can be explained by the enhanced subauroral electric field, except the directions of the dawnside meridional electric field, FACs and plasma flow are opposite to those on the dusk side. However, critical questions remain to be answered: Are dawnside SAPS also driven by current closure in the ionosphere? What are the dawnside ring current and FAC distributions when dawnside SAPS occur during major storms? How are the dawnside currents different from the duskside ones during typical SAPS events? What is the role of the strong solar wind and IMF driving conditions in generating dawnside SAPS?

These questions are also critical to understanding whole geospace coupling, especially during major storms which could cause severe adverse effects in human society and infrastructure. One of the important aspects of space weather is dawn-dusk asymmetry of these powerful events. For instance, Ohtani et al. (2018) reported highly deflected geomagnetic field on the ground in the morningside mid-latitudes during four intense geomagnetic storms, which caused unusual geomagnetically induced current (GIC) events. Ohtani et al. (2018) analyzed the ground-based magnetometer measurements to reveal the formation of a dawnside current wedge system. In this current system, the westward electrojet in the dawnside ionosphere is fed by an unbalanced downward FAC at its eastward edge and is drained by an unbalanced upward current at its westward edge. Ohtani (2021) additionally demonstrated that this current system is a characteristic feature of the magnetosphere-ionosphere coupling during the storm main phase. Furthermore, the dawnside current wedge was shown to correspond to a configuration in which the westward electrojet on the dawnside was more intense compared to the eastward electrojet on the duskside, while the equatorial magnetospheric current had the opposite dawn-dusk asymmetry: it was stronger on the duskside than on the dawnside. While in this paper we do not demonstrate a direct relationship between the dawnside current wedge system and dawnside SAPS, both represent intrinsic dawn-dusk asymmetry of the geospace system during intense storms.

In this study, we address the science questions raised above and uncover the driving mechanisms of dawnside SAPS observed during the super storm on 20 November 2003 with observational data from DMSP satellites and simulations using the Multiscale Atmosphere-Geospace Environment (MAGE) model (Pham et al., 2022). The MAGE model was recently used to resolve the mesoscale structure of and self-consistently characterize the magnetosphere-ionosphere coupling during SAPS (Lin et al., 2021). We compare auroral precipitation, ionospheric ion drifts, and magnetic perturbations between the dawn and dusk sides, and between different stages of the storm from both observations and model simulations. The formation of dawnside SAPS is attributed to the strong convection electric field in the magnetosphere which enables plasma sheet ions to access the dawnside inner magnetosphere and build up the ring current pressure there. Substantial upward Region-2 FACs develop inside the electron plasmasheet boundary as a result of the azimuthal pressure gradient and ultimately drive the dawnside SAPS. Test particle simulations and controlled numerical experiments are carried out to further demonstrate the dependence of ion drifts and dawnside SAPS on the strength of the magnetospheric convection.

2 Model setup

MAGE is a newly developed geospace model that was designed in particular to resolve and study mesoscale structures during storms, such as SAPS (Lin et al., 2021), traveling ionospheric disturbances (Pham et al., 2022), and plasma sheet bursty bulk flows (K. Sorathia et al., 2021). The MAGE configuration used in the present study couples the Grid Agnostic MHD for Extended Research Applications (GAMERA) global MHD model of the magnetosphere (B. Zhang et al., 2019; K. Sorathia et al., 2020), the Rice Convection Model (RCM) model of the ring current (Toffoletto et al., 2003), Thermosphere Ionosphere Electrodynamics General Circulation Model (TIEGCM) of the upper atmosphere (Richmond et al., 1992), and the RE-developed Magnetosphere-Ionosphere Coupler/Solver (REMIX) (Merkin & Lyon, 2010). GAMERA is a new MHD model based on the algorithms underlying the high-heritage Lyon-Fedder-Mobbary (LFM) model (Lyon et al., 2004). Furthermore, MAGE carries on the legacy of an earlier coupled geospace model developed by the same group (e.g., Lin et al., 2019), but is based on an entirely new coupling infrastructure.

In this study, MAGE uses a moderate grid resolution which is sufficient for resolving the mesoscale structure of SAPS (Lin et al., 2021). Specifically, GAMERA uses $96\times 96\times 128$ grid cells in the radial, meridional, and azimuthal directions, respectively, where the spherical symmetry axis of the grid is pointing from Earth to Sun. The radial grid spacing is $\sim 0.2\ R_E$ near the inner boundary, which is set at $1.5\ R_E$. RCM uses $180\times 360\times 115$ grid cells in the latitudinal, longitudinal (in Solar Magnetic, SM, coordinates), and energy dimensions, respectively. The RCM grid has a resolution of $0.25°$ in latitude and $1°$ in longitude. In the energy dimension, there are 29 energy channels for electrons, 85 energy channels for protons, and 1 zero-energy channel for the cold plasmasphere. The energy invariants of these channels correspond to electron kinetic energy of $\sim$10 eV to $\sim$10 keV and ion kinetic energy of 10s eV to $\sim$100 keV at the geosynchronous orbit. The energy grid has a good coverage of the typical energy range of ions consisting the ring current and electrons that contribute to the diffuse electron precipitation. REMIX grid uses 55 x 360 grid cells in the latitudinal and longitudinal directions (in SM), respectively. Its resolution is $1.0°$ in both dimensions and the low latitude boundary is at $35°$ magnetic latitude (MLAT). TIEGCM uses $288\times 144\times 57$ cells in longitudinal, latitudinal, and altitudinal directions (in geographic coordinate system), respectively. It has a uniform horizontal resolution of $1.25°$ and a vertical pressure grid of 0.25 scale height. GAM-

ERA and TIEGCM both adopt a ring-average technique to treat the singularity at the spherical axes of their respective grids (B. Zhang et al., 2019b; Dang et al., 2021). GAMERA and RCM exchange information every 10 s, GAMERA and REMIX every 5 s, and REMIX and TIEGCM every 5 s.

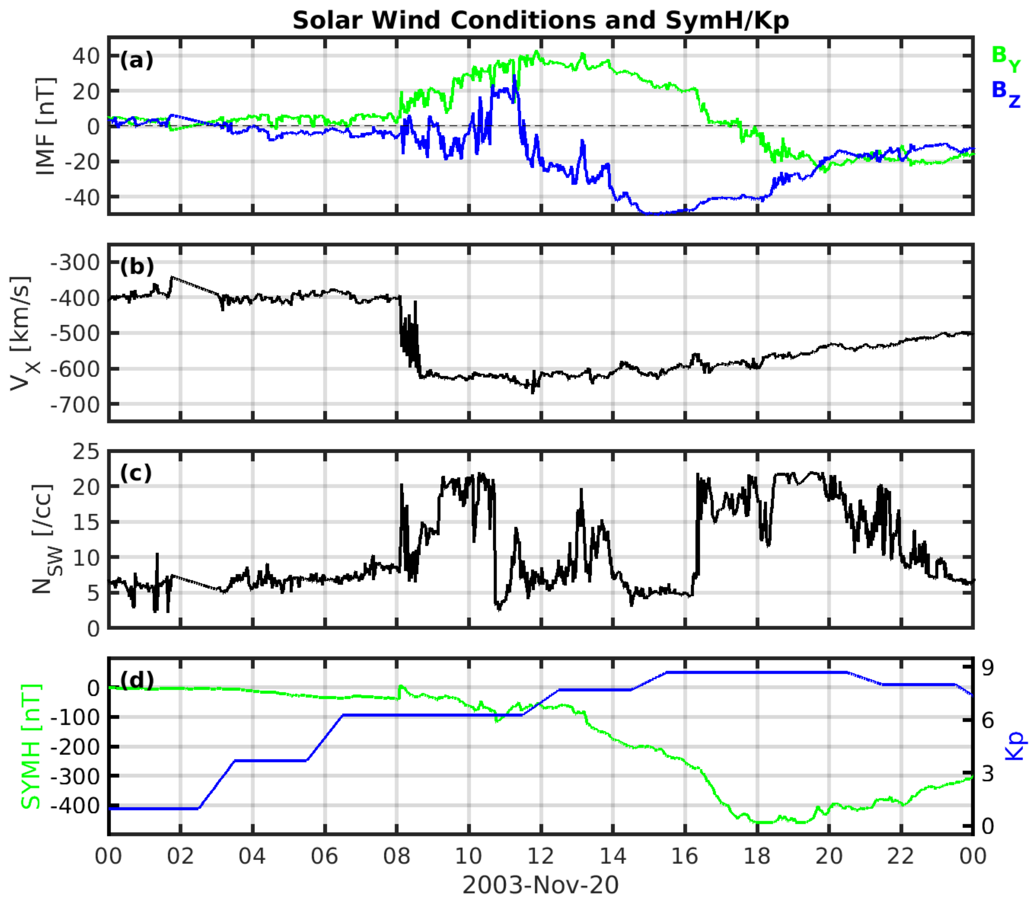

Figure 1. Solar wind/IMF and SYMH/Kp geomagnetic indices during 20 November 2003. (a) IMF B_Y (green) and B_Z (blue) in Geocentric Solar Magnetospheric System (GSM) coordinates. (b) Solar wind velocity GSM V_X. (c) Solar wind density. (d) SYMH (green) and Kp indices (blue).

Figures 1a-1d show the solar wind/interplanetary magnetic field (IMF) conditions and SYMH/Kp geomagnetic activity indices during 20 November 2003. The data were obtained from the CDAWeb OMNI data base. The solar wind and IMF data were used to drive the MAGE model. A coronal mass ejection (CME) arrived at the Earth at around 08 UT on 20 November 2003. The solar wind speed was over 600 km/s for the next 8 hours. The solar wind density reached 20/cc, greatly enhancing the dynamic pressure impacting on the magnetosphere. Strong IMF started to impact the magnetosphere with a negative B_Z as large as -20 nT in the first two hours after the sudden storm commencement and enhanced to -50 nT by 15 UT. IMF B_Y also gradually increased to +40 nT during the main phase and then turned to -20 nT in the recovery phase. The SYMH index reached a minimum of -457 nT at around 18 UT after which it gradually recovered.

3 Observations and simulation results

3.1 Structure of dawnside SAPS

Figures 2a-2e show an example of SAPS observed by the DMSP F16 satellite during its crossing of the northern high-latitude ionosphere from 13:51 UT to 14:31 UT. From top to bottom are DMSP measurements of electron precipitation energy spectrum, integrated electron precipitation energy flux ($EnFlux$), cross-track ion drift velocity (V_{HORZ}), electron density, cross-track magnetic perturbation (dB_Z), and the derived FAC density. The data are smoothed with a 15 s moving mean window to emphasize structures on the scale of ∼100 km and larger. The vertical dashed lines show the time when $EnFlux$ drops to 0.2 mW/m^2 and are used to indicate the equatorward electron precipitation boundaries. Subauroral regions equatorward of those boundaries and poleward of 35° MLAT are shaded with the magenta color. FAC densities are calculated from dB_Z by using Ampere's Law, assuming a one-dimensional current sheet (e.g., Higuchi & Ohtani, 2000; Kilcommons et al., 2017; Xiong et al., 2014). In the northern hemisphere, downward FACs are positive and upward FACs are negative. The green shaded regions highlight the upward FACs on the dawnside and downward FACs on the duskside, which are Region-2 currents. The FAC boundaries are estimated with a threshold value of 0.05 $\mu A/m^2$. Note that the FACs show alternating upward and downward signatures on the duskside, which imply finer structures embedded in the large-scale Region-1/Region-2 FACs (e.g., Xiong et al., 2014; Liu et al., 2021). Small scale FAC structures away from the equatorward auroral boundaries are not shaded for better visibility.

Figure 2c shows a separate sunward (westward) ion drift channel on the duskside around 13:58 UT with a peak value of nearly 1.6 km/s, marked with the thick blue horizontal bar. This is a typical duskside SAPS structure that has been widely observed and studied. More interestingly, there are also strong plasma flows on the dawnside equatorward of electron auroral boundary at about 56° MLAT. This flow has a magnitude of up to 1 km/s in the sunward/eastward direction. These dawnside subauroral flow structures are hereinafter referred to as the dawnside SAPS. Note that Horvath and Lovell (2021) showed several examples of dawnside SAPS observed by DMSP F13 only. Here we have examined all available DMSP data on 20 November 2003 that provide additional evidence for the dawnside SAPS observed by DMSP F13, F14, and F15 in the Supporting Information (Figures S1, S2, and S3). The dawnside SAPS are also collocated with the low-latitude part of Region-2 FACs, which are upward on the dawnside. While the electron density data show a trough structure collocated with the SAPS channel on the duskside, it does not show an apparent trough on the dawnside. An electron density trough forms in the premidnight sector due to the opposite directions of convection and corotation. Plasma flux tubes thus can stay much longer in the subauroral region for the plasma density to be depleted by recombination. On the dawnside, however, convection and corotation are along the same direction thus not favoring plasma depletion to form a trough structure (Spiro et al., 1978; Moffett & Quegan, 1983; Rodger et al., 1992). This is probably why the dawnside SAPS do not show a distinct channel as the dusk SAPS do.

Figures 2f-2h show the MAGE model outputs of $EnFlux$, V_{HORZ}, and FAC density sampled along DMSP F16 trajectory during the same time interval. The sampled simulation results are also smoothed with a 15 s moving mean to remove small-scalle fluctuations. Using a similar format in Figure 2b, Figure 2g shows a duskside SAPS flow channel at ∼ 19.5 magnetic local time (MLT) and ∼ 50° MLAT with a peak speed of ∼ 1.2 km/s. On the dawnside, eastward subauroral flows are visible at around 8.6 MLT and ∼ 54° MLAT, with a peak speed of ∼ 1.0 km/s. Both the duskside and dawnside SAPS are collocated with the low latitude part of Region-2 FACs, which are downward on the duskside and upward on the dawnside.

Figures 2i and 2j illustrate the SAPS generation processes by showing the northern hemispheric distributions of zonal ion drift at 13:57 UT and 14:22 UT when DMSP

F16 was located inside the duskside and dawnside SAPS, respectively. Here, the zonal drift is viewed from above the north pole and defined as positive for the eastward flow. The magenta curve shows the equatorward auroral boundary, which is identified by finding at each MLT where $EnFlux$ drops to below 0.2 mW/m^2. The cyan and green curves show the equatorward boundaries of downward and upward FACs, respectively, where the FAC density magnitude drops to below 0.05 $\mu A/m^2$ at each MLT. For instance, at 13:57 UT, a SAPS channel, i.e., enhanced plasma flow equatorward of the auroral boundary, can be seen on the duskside from 17 MLT to $\sim$ 22 MLT at around 50° MLAT, and on the dawnside from 0 MLT to about 10 MLT slightly above 50° MLAT. The FAC equatorward boundaries are located at a lower latitude than the electron precipitation equatorward boundaries on both the duskside and dawnside. As a result of current closure, strong poleward and equatorward electric fields are produced in the low conductance subauroral regions, which drive westward and eastward SAPS on the duskside and dawnside, respectively.

Note that the simulated integrated electron precipitation energy flux on the dawnside is more than 20 mW/m^2, which is obviously overestimated compared to DMSP measurements. We attribute this to the electron precipitation model used in this MAGE simulation, where a uniform and constant electron loss rate is applied when deriving the diffuse electron precipitation (Lin et al., 2021). However, the overestimated electron precipitation should not affect the dawnside SAPS fundamentally except introducing a latitudinal minimum in V_{HORZ}. The equatorward electric field that drives the eastward subauroral flow is determined by the large scale upward Region-2 FACs which requires closing via the equatorward Pedersen currents from the downward Region-1 FACs at higher latitudes. A stronger precipitation energy flux can nevertheless generate a latitudinally narrow high ionospheric conductance band and hence a weaker equatorward electric field and a weaker eastward zonal drift, forming a separate flow channel-like distribution of ion drifts in the simulation results.

3.2 Occurrence of dawnside SAPS

Figures 3a and 3b compare the SAPS structures detected by DMSP F13 during quiet time and storm time to understand the occurrence of dawnside SAPS. Figure 3a shows the cross track ion drift from 06:22 UT to 06:52 UT before the sudden storm commencement when SAPS already occurred on the duskside but not on the dawnside. Note here we only show the V_{HORZ} data to focus on the SAPS structures as the analysis method has been demonstrated in Figure 2. Details about FAC, electron precipitation, and electron density are provided in the Supporting Information as Figures S4-S7. Between the equatorward boundaries of electron precipitation and Region-2 FACs are SAPS indicated by the blue horizontal bar. On the dawnside, however, there is only a very narrow region of upward Region-2 FACs equatorward of the electron precipitation boundary, where the FAC density is only slightly above the threshold value of 0.05 $\mu A/m^2$. The V_{HORZ} data also shows only negligible horizontal drifts. Therefore, we infer no dawnside SAPS at around 06:30 UT before the sudden storm commencement.

Figure 3b shows V_{HORZ} measured from 18:15 UT to 18:45 UT when the SYMH index was near its minimum. A separate SAPS channel is clearly visible on the duskside with a peak speed of $\sim$1.2 km/s. The auroral boundary moved equatorward by about 15° at this MLT of around 18. On the dawnside, a substantial eastward SAPS channel is also identifiable with a peak speed of more than 1 km/s, similar to the one showed in Figure 2. Note in Figure 3b the green shaded area indicating upward Region-2 FACs is overlapping with the magenta shading.

Figures 3c and 3d show the MAGE simulation results for the same two intervals. Similarly, SAPS already occurred on the duskside but not on the dawnside at around

06:30 UT. Whereas in the main phase, substantial SAPS with peak speeds of more than 1 km/s are found on both the duskside and dawnside.

Both the DMSP data and MAGE simulation results reveal that the most important change related to the occurrence of dawnside SAPS was the location of the equatorward FAC boundary relative to the equatorward precipitation boundary. Figures 3e and 3f provide a more illustrative view of the SAPS evolution during the storm with MAGE simulated zonal ion drifts at 06:30 UT and 18:30 UT, respectively. The format is similar to that in Figures 2i and 2j. Before the storm started, the upward Region-2 FAC boundary was very close to the auroral boundary on the dawnside, which was also located at a lower latitude than on the duskside. Refer to the green and magenta curves in Figure 3e. Therefore, there were no dawnside SAPS formed there. When the storm activity level reached its peak, both the upward Region-2 FAC boundary and the auroral boundary extended equatorward. However, the FAC boundary moved equatorward by several more degrees than the auroral boundary equatorward expansion, and dawnside SAPS formed in the gap between the two boundaries. Refer to the green and magenta curves in Figure 3f and also the red belt between the two boundaries representing the eastward SAPS channel.

The Region-2 FACs are mainly driven by the azimuthal pressure gradient in the inner magnetosphere (e.g., Vasyliunas, 1970). Figures 3g and 3h show the northern ionospheric FAC distribution at 06:30 UT and 18:30 UT, respectively, where positive currents are downward and negative currents are upward. Note that the color scale is twice larger in Figure 3h than in Figure 3g. The upward Region-2 FACs on the dawnside are thus much stronger at 18:30 UT than at 06:30 UT. Figures 3i-3j show the plasma pressure distributions in the magnetospheric equatorial plane on a logarithmic scale. Note here that the color scale is one order of magnitude higher in Figure 3h for 18:30 UT when the ring current pressure was significantly enhanced. The black curves show plasma pressure contours separated by 2 nPa in Figure 3i and by 20 nPa in Figure 3j, which imply a substantial increase in pressure gradient at 18:30 UT compared to 06:30 UT. In particular, the azimuthal pressure gradient was greatly enhanced at almost all MLTs at 18:30 UT, which should account for the substantial strengthening of upward Region-2 FACs and the occurrence of dawnside eastward SAPS in the storm main phase as shown in Figures 3f and 3h.

3.3 Origin of dawnside SAPS

To better understand how the ring current and Region-2 FACs develop on the dawn and dusk sides, we analyze the ring current pressure and ion convection drift with the RCM simulation results. Figures 4a and 4b show the the ring current partial pressure as a function of proton energy and UT in the dusk and dawn. The pressure is sampled at the geosynchronous orbit of $L = 6.6$ at 18 MLT and 06 MLT, respectively. Figure 4a shows that the duskside ring current pressure started to build up at around 5 UT when IMF B_Z turned southward. However, Figure 4b shows that the dawnside ring current pressure from above 10 keV does not dramatically enhance until ∼08:45 UT when the solar wind speed jumped to more than 600 km/s. The simulation results suggest that the total ring current pressure is predominantly contributed by protons with energies from 10 keV to 100 keV during the storm main and recovery phases, which is consistent with the recent observational finding by Zhao et al. (2015)

The distinct responses of 10-100 keV energetic protons on the duskside and dawnside are responsible for the different occurrences of SAPS on the two sides as discussed in Section 3.2. Transport of energetic ions in the inner and middle magnetosphere can be well described by adiabatic particle motion theory (e.g., Wolf, 1983). The particle kinetic energy increases during the adiabatic transport toward the inner magnetosphere as $\lambda = WV^{2/3}$ is conserved along the drift path. Here λ is an energy invariant, W is the particle kinetic energy, and V is the flux tube volume defined as $\int_{sh}^{nh} \frac{ds}{B}$ (Toffoletto et al., 2003). While energy-dependent magnetic curvature and gradient drifts deflect the ions westward toward the duskside, they can be transported to the dawnside when the $\vec{E}\times\vec{B}$ convection is stronger (Korth et al., 1999). Figures 4c and 4d illustrate the transition from a configuration dominated by magnetic drift during relatively quiet time to that dominated by the electric drift during storm time. The colorbar shows the ratio between the $\vec{E}\times\vec{B}$ drift speed ($|V_{\vec{E}\times\vec{B}}|$) and the magnetic drift speed ($|V_{R_C,\nabla B}|$) derived from RCM outputs for ions with the same energy invariant $\lambda = 1139.0$. These ions have kinetic energies of a few keV when they are in the plasma sheet $X \sim -15\ R_E$. The cyan curves indicate where their kinetic energy reaches 10 keV and 100 keV during the adiabatic transport to the inner magnetosphere. With a logarithmic scale, positive values show where the electric drift is dominant and negative values show where the magnetic drift is dominant. It can be seen that ions are dominated by the magnetic drifts at 06:30 UT and by the $\vec{E} \times \vec{B}$ drift at 18:30 UT as they are energized to typical ring current levels (10-100 keV). The magenta curves show the contour of the total effective potential (Toffoletto et al., 2003) separated by 20 kV for the chosen energy invariant, which are equivalent to the drift path. During relatively weak convection, energetic ions seldom reach the dawnside. Whereas during strong convection, a larger cross-section of the magnetotail can now drift to the dawnside. Note the comparison between quiet time and storm time is also valid for ions with other energy invariants. See Figure S8 in the Supporting Information for $\lambda = 338.2$ and $\lambda = 3032.9$. The fiducial energy channel of $\lambda = 1139.0$ is chosen because on average ions in this channel contribute the most to the total ring current pressure.

To further verify the dependence of energetic proton drifts on the strength of magnetospheric convection and their connection to the Region-2 FACs, we traced the trajectories of protons with a test particle model using the electromagnetic fields from the MAGE simulation. The test particle model used was the Conservative Hamiltonian Integrator of Magnetospheric Particles (CHIMP) model described in detail by Ukhorskiy et al. (2015), K. Sorathia et al. (2017), and K. A. Sorathia et al. (2018). We consider protons with initial energies between 1 and 50 keV. Test particles were released from the nightside equatorial plane between 21 MLT and 3 MLT at a radial distance between 14.5 R_E and 15.5 R_E. In the two CHIMP runs, protons were released at 6 UT and 18 UT, when the magnetospheric convection was very weak before the sudden storm commencement and when it was greatly enhanced during the main phase, respectively. Figures 4e and 4f show the distributions of test particle protons and background residual magnetic field dB_Z with dipole subtracted in the equatorial plane 30 minutes after they were released. The purple circles represent protons that were active near the equatorial plane with the size of the circles proportional to the particle energy. The green and cyan curves indicate the upward and downward FAC boundaries and the magenta curves indicate the equatorward auroral boundaries shown in Figures 3g-3h that are mapped to the magnetosphere.

In the first CHIMP simulation, protons released at 6 UT mostly drifted westward and were accelerated toward the duskside. Figure 4e shows that a number of 10-100 keV protons were transported toward the downward Region-2 FACs, i.e., the region enclosed by the cyan curve. However, few energetic protons were seen in the dawnside upward Region-2 FACs, i.e., the region enclosed by the green curve. Accordingly, SAPS were only generated on the duskside between the inner boundaries of downward Region-2 FACs (cyan curve) and electron precipitation (magenta curve). In the second CHIMP simulation, protons released at 18 UT experienced a much stronger magnetospheric convection electric field. Figure 4f shows that significant amount of energetic protons accessed both the downward and upward Region-2 FACs on the duskside and dawnside, respectively. The inner boundaries of upward and downward Region-2 FACs are much closer to Earth than the inner electron precipitation boundary in both dawn and dusk, leaving SAPS formed in the gaps. The test particle proton trajectories are consistent with the streamlines derived from the effective total potential discussed in Figures 4c-4d. Evolution of the test particle motion is shown in the Supporting Information Movie S1 and S2. Note the inner magnetospheric magnetic field was greatly enhanced at 18:30 UT compared to 06:30 UT, which was expected to reduce both magnetic and electric drift speeds. The transition of dominance from magnetic drift to electric drift is mainly attributed to the enhancement of electric field.

4 Discussion

The comparison between 06:30 UT and 18:30 UT in Figure 3 indicates the importance of strong convection in the formation of dawnside SAPS. The dawnside SAPS had not been discussed until the recent work by Horvath and Lovell (2021) and Huang et al. (2021), probably because the necessary strong convection does not occur very often. During weak and moderate storms dawnside ring current build-up is less efficient so that there are insufficient subauroral upward Region-2 FACs to produce noticeable dawnside SAPS. The dependence of energetic ring current ion access to the dawnside on strong solar wind driving conditions is also supported by satellite observations. In the Supporting Information Figure S9, we show the energetic proton flux in the range of 50-400 keV measured by the LANL L1, L4, and L7 satellites during 20 November 2003. The energetic proton flux data show a clear difference between the dawnside and duskside. The duskside energetic proton flux reached a high level under both northward and southward IMF conditions, covering a much broader range of geomagnetic activity levels. Whereas the dawnside energetic proton flux distribution with IMF B_Z shows much more significant preference to strong southward IMF conditions when the magnetospheric convection was expected to be much stronger.

In a controlled MAGE experiment shown in the Supporting Information Figure S10, we artificially reduced all IMF components by a factor of ten while maintaining the same solar wind parameters. The reduced IMF has its strongest southward B_Z of -5 nT, which is expected to trigger a much weaker storm. With greatly reduced magnetospheric convection, the duskside SAPS still occurred but the dawnside SAPS did not occur even during the storm main phase. The dawnside ring current pressure was also much weaker and closer to the equatorward auroral boundary. This controlled experiment provides an additional support for the dependence of dawnside SAPS on storm activity level.

Ohtani et al. (2018) reported a list of major storms (Dst minimum $<$ -100 nT) in their analysis of dawnside intensification of auroral electrojet and FACs (Table 1 in Ohtani et al. (2018)). The events were characterized by the ten largest hourly ground magnetic perturbations on record. We examined the DMSP data for these events. Dawnside SAPS were also found during those strong storm events except relatively weak dawnside SAPS signatures in the storm on 7 January 2005 which had a Dst minimum of -71 nT and should be classified as a moderate storm, and in the storm on 22 October 2001 which had a Dst minimum of -177 nT. A statistical survey of dawnside SAPS is necessary to better understand their occurrence with a more detailed description of their dependence on the storm activity level.

IMF B_Y was also very strong in the 20 November 2003 event. IMF B_Y increased to a maximum of positive 40 nT at around 12 UT during the early main phase. A strong IMF B_Y is known to cause a substantial dawn-dusk asymmetry of the coupled magnetosphere-ionosphere, (e.g., Shepherd & Ruohoniemi, 2000; Holappa et al., 2020; Kumar et al., 2020). We conducted another controlled experiment using a MAGE simulation in which IMF B_Y was artificially reduced to zero while other solar wind and IMF parameters were the observed values, which is shown in the Supporting Information as Figure S11. The dawnside SAPS still occurred in this case despite a more dawn-dusk symmetric convection and FAC pattern. At 18:30 UT when the storm reached the strongest level as indicated by the SYMH index, substantial eastward subauroral plasma flow appeared in the dawn sector with a peak speed of ~ 2 km/s. Therefore, IMF B_Y is not the determining factor for the generation of dawnside SAPS.

It is necessary to clarify that the dawnside SAPS studied in this work are different from the recently reported dawnside polarization streams (DAPS) by Liu et al. (2020). Both DAPS and dawnside SAPS occur on the dawnside and refer to the enhanced eastward plasma flows. But DAPS occur above the poleward auroral boundary inside the polar cap while dawnside SAPS occur equatorward of the auroral boundary at subauroral latitudes. Dawnside SAPS only occur during major geomagnetic storms while DAPS do not require strong geomagnetic activity.

There have also been reports of eastward subauroral plasma flows, (e.g., Ebihara et al., 2008; Voiculescu & Roth, 2008; Lileo et al., 2010; Horvath & Lovell, 2018), which are called abnormal SAPS or abnormal SAID. The eastward drifts and equatorward electric fields of abnormal SAPS were suggested to be associated with the so-called over-shielding effects, i.e. Region-2 FACs dominating over Region-1 FACs due to IMF northward turning or reduced convection under southward IMF. These abnormal cases occur in the dusk or premidnight sectors under relatively weak driving conditions and are thus different from the dawnside SAPS during major storms investigated in this study.

5 Conclusion

In this study we investigated the origin of dawnside SAPS during major geomagnetic storms. The dawnside SAPS consist of similar features to the typical SAPS on the duskside, including substantial Region-2 FACs extending to the equatorward side of the auroral low latitude boundary, and an enhanced meridional electric field in the subauroral ionosphere that drives fast plasma flows toward the dayside. The dawnside SAPS occur during major geomagnetic storms when the magnetospheric convection is sufficiently strong. Energetic ring current ions are transported toward the dawnside and more inward than the electron plasmasheet boundary. Dawnside SAPS can be then generated by the intensified upward Region-2 FACs that are connected to the dawnside subauroral ionosphere. The characteristic dependence of magnetospheric and ionospheric plasma and currents on the convection level revealed in this study is an importance advance in our understanding of geospace response to very strong solar wind driving conditions, which could better prepare us for potential extreme space weather events.

Data Availability Statement

The MAGE simulation data used for dawnside SAPS analysis in the study are available at the NCAR Digit Assets Service Hub via https://doi.org/10.5065/f8z0-0p03 (Lin et al., 2022).

Acknowledgments

Dong Lin was supported by the Advanced Study Program (ASP) Postdoctoral Fellowship of National Center for Atmospheric Research (NCAR). NCAR is sponsored by National Science Foundation (NSF). This work is supported by NASA GCR grant 80NSSC17K0013, DRIVE Science Center for Geospace Storms (CGS) under grant 80NSSC20K0601, LWS grants 80NSSC20K0356, 80NSSC19K0080, 80NSSC17K0679, 80NSSC21K0008, 80NSSC21K1677, and 80NSSC20K0199, NSF CEDAR grant 2033843. CSH at the Air Force Research Laboratory is supported by NASA grants 80HQTR20T0015 and 80HQTR20T0016. MO is supported by NASA LWS grant 80NSSC19K0080. KS is supported by NASA 80NSSC19K0241 and 80NSSC20K1833. QW is supported by NASA LWS 80NSSC20K0199, NNX17AG69G, and 80NAAC21K0014. YZ is supported by NASA grant 80NSSC20K0354. We would like to acknowledge high-performance computing support from Cheyenne (doi:10.5065/D6RX99HX) provided by NCAR's Computational and Information Systems Laboratory. Dong Lin is

thankful to Dr. Gang Lu for the internal review. The OMNI data are available at https://cdaweb.gsfc.nasa.gov/index
The DMSP SSJ and SSIES data are obtained from http://cedar.openmadrigal.org/.

References

Aa, E., Erickson, P. J., Zhang, S.-R., Zou, S., Coster, A. J., Goncharenko, L. P., & Foster, J. C. (2020). A statistical study of the subauroral polarization stream over north american sector using the millstone hill incoherent scatter radar 1979–2019 measurements. *Journal of Geophysical Research: Space Physics*, *125*(10), e2020JA028584. doi: 10.1029/2020JA028584

Anderson, B., Ohtani, S.-I., Korth, H., & Ukhorskiy, A. (2005). Storm time dawn-dusk asymmetry of the large-scale birkeland currents. *Journal of Geophysical Research: Space Physics*, *110*(A12). doi: 10.1029/2005JA011246

Anderson, P., Carpenter, D., Tsuruda, K., Mukai, T., & Rich, F. (2001). Multisatellite observations of rapid subauroral ion drifts (said). *Journal of Geophysical Research: Space Physics*, *106*(A12), 29585–29599. doi: 10.1029/2001JA000128

Anderson, P., Hanson, W., Heelis, R., Craven, J., Baker, D., & Frank, L. (1993). A proposed production model of rapid subauroral ion drifts and their relationship to substorm evolution. *Journal of Geophysical Research: Space Physics*, *98*(A4), 6069–6078. doi: 10.1029/92JA01975

Califf, S., Li, X., Wolf, R., Zhao, H., Jaynes, A., Wilder, F., ... Redmon, R. (2016). Large-amplitude electric fields in the inner magnetosphere: Van allen probes observations of subauroral polarization streams. *Journal of Geophysical Research: Space Physics*, *121*(6), 5294–5306. doi: 10.1002/2015JA022252

Dang, T., Zhang, B., Lei, J., Wang, W., Burns, A., Liu, H.-l., ... Sorathia, K. A. (2021). Azimuthal averaging–reconstruction filtering techniques for finite-difference general circulation models in spherical geometry. *Geoscientific Model Development*, *14*(2), 859–873. doi: 10.5194/gmd-14-859-2021

Ebihara, Y., & Ejiri, M. (2000). Simulation study on fundamental properties of the storm-time ring current. *Journal of Geophysical Research: Space Physics*, *105*(A7), 15843–15859. doi: 10.1029/1999JA900493

Ebihara, Y., Nishitani, N., Kikuchi, T., Ogawa, T., Hosokawa, K., & Fok, M.-C. (2008). Two-dimensional observations of overshielding during a magnetic storm by the super dual auroral radar network (superdarn) hokkaido radar. *Journal of Geophysical Research: Space Physics*, *113*(A1). doi: 10.1029/2007JA012641

Fok, M.-C., Moore, T. E., & Greenspan, M. E. (1996). Ring current development during storm main phase. *Journal of Geophysical Research: Space Physics*, *101*(A7), 15311–15322. doi: 10.1029/96JA01274

Foster, J., Erickson, P., Coster, A., Goldstein, J., & Rich, F. (2002). Ionospheric signatures of plasmaspheric tails. *Geophysical Research Letters*, *29*(13), 1–1. doi: 10.1029/2002GL015067

Foster, J., Erickson, P., Lind, F., & Rideout, W. (2004). Millstone hill coherent-scatter radar observations of electric field variability in the sub-auroral polarization stream. *Geophysical research letters*, *31*(21). doi: 10.1029/2004GL021271

Gonzalez, W., Joselyn, J.-A., Kamide, Y., Kroehl, H. W., Rostoker, G., Tsurutani, B., & Vasyliunas, V. (1994). What is a geomagnetic storm? *Journal of Geophysical Research: Space Physics*, *99*(A4), 5771–5792. doi: 10.1029/93JA02867

He, F., Zhang, X.-X., & Chen, B. (2014). Solar cycle, seasonal, and diurnal variations of subauroral ion drifts: Statistical results. *Journal of Geophysical Research: Space Physics*, *119*(6), 5076–5086. doi: 10.1002/2014JA019807

Higuchi, T., & Ohtani, S.-i. (2000). Automatic identification of large-scale field-aligned current structures. *Journal of Geophysical Research: Space Physics*, *105*(A11), 25305–25315. doi: 10.1029/2000JA900073

Holappa, L., Asikainen, T., & Mursula, K. (2020). Explicit imf dependence in geomagnetic activity: Modulation of precipitating electrons. *Geophysical Research Letters*, *47*(4), e2019GL086676. doi: 10.1029/2019GL086676

Horvath, I., & Lovell, B. C. (2018). Investigating the development of abnormal subauroral ion drift (asaid) and abnormal subauroral polarization stream (asaps) during the magnetically active times of september 2003. *Journal of Geophysical Research: Space Physics*, *123*(2), 1566–1582. doi: 10.1002/2017JA024870

Horvath, I., & Lovell, B. C. (2021). Investigating the coupled magnetosphere-ionosphere-thermosphere (m-i-t) system's responses to the 20 november 2003 superstorm. *Journal of Geophysical Research: Space Physics*, e2021JA029215. doi: 10.1029/2021JA029215

Huang, C.-S., Zhang, Y., Wang, W., Lin, D., & Wu, Q. (2021). Low-latitude zonal ion drifts and their relationship with subauroral polarization streams and auroral return flows during intense magnetic storms. *Journal of Geophysical Research: Space Physics*, e2021JA030001. doi: 10.1029/2021JA030001

Kilcommons, L. M., Redmon, R. J., & Knipp, D. J. (2017). A new dmsp magnetometer and auroral boundary data set and estimates of field-aligned currents in dynamic auroral boundary coordinates. *Journal of Geophysical Research: Space Physics*, *122*(8), 9068–9079. doi: 10.1002/2016JA023342

Korth, H., Thomsen, M., Borovsky, J., & McComas, D. (1999). Plasma sheet access to geosynchronous orbit. *Journal of Geophysical Research: Space Physics*, *104*(A11), 25047–25061. doi: 10.1029/1999JA900292

Kumar, S., Veenadhari, B., Chakrabarty, D., Tulasi Ram, S., Kikuchi, T., & Miyoshi, Y. (2020). Effects of imf by on ring current asymmetry under southward imf bz conditions observed at ground magnetic stations: Case studies. *Journal of Geophysical Research: Space Physics*, *125*(10), e2019JA027493. doi: 10.1029/2019JA027493

Kunduri, B., Baker, J., Ruohoniemi, J., Thomas, E., Shepherd, S., & Sterne, K. (2017). Statistical characterization of the large-scale structure of the subauroral polarization stream. *Journal of Geophysical Research: Space Physics*, *122*(6), 6035–6048. doi: 10.1002/2017JA024131

Landry, R. G., & Anderson, P. C. (2018). An auroral boundary-oriented model of subauroral polarization streams (saps). *Journal of Geophysical Research: Space Physics*, *123*(4), 3154–3169. doi: 10.1002/2017JA024921

Lileo, S., Karlsson, T., & Marklund, G. T. (2010). Statistical study on the occurrence of asaid electric fields. In *Annales geophysicae* (Vol. 28, pp. 439–448). doi: 10.5194/angeo-28-439-2010

Lin, D., Sorathia, K., Wang, W., Merkin, V., Bao, S., Pham, K., … others (2021). The role of diffuse electron precipitation in the formation of subauroral polarization streams. *Journal of Geophysical Research: Space Physics*, *126*(12), e2021JA029792. doi: 10.1029/2021JA029792

Lin, D., Wang, W., Merkin, V. G., Huang, C., Oppenheim, M., Sorathia, K., … Garretson, J. (2022). Data repository for lin et al. (2022) "origin of dawnside subauroral polarization streams during major geomagnetic storms". *UCAR/NCAR - DASH Repository*. doi: 10.5065/f8z0-0p03

Lin, D., Wang, W., Scales, W. A., Pham, K., Liu, J., Zhang, B., … Maimaiti, M. (2019). Saps in the 17 march 2013 storm event: Initial results from the coupled magnetosphere-ionosphere-thermosphere model. *Journal of Geophysical Research: Space Physics*, *124*(7), 6212–6225. doi: 10.1029/2019JA026698

Liu, J., Lyons, L., Wang, C.-P., Hairston, M., Zhang, Y., & Zou, Y. (2020). Dawnside auroral polarization streams. *Journal of Geophysical Research: Space Physics*, *125*(8), e2019JA027742. doi: 10.1029/2019JA027742

Liu, J., Lyons, L., Wang, C.-P., Ma, Y., Strangeway, R., Zhang, Y., … Khurana,

K. (2021). Embedded regions 1 and 2 field-aligned currents: Newly recognized from low-altitude spacecraft observations. *Journal of Geophysical Research: Space Physics*, *126*(6), e2021JA029207. doi: 10.1029/2021JA029207

Lyon, J., Fedder, J., & Mobarry, C. (2004). The lyon–fedder–mobarry (lfm) global mhd magnetospheric simulation code. *Journal of Atmospheric and Solar-Terrestrial Physics*, *66*(15-16), 1333–1350. doi: 10.1016/j.jastp.2004.03.020

Merkin, V., & Lyon, J. (2010). Effects of the low-latitude ionospheric boundary condition on the global magnetosphere. *Journal of Geophysical Research: Space Physics*, *115*(A10). doi: 10.1029/2010JA015461

Mishin, E., & Blaunstein, N. (2008). Irregularities within subauroral polarization stream-related troughs and gps radio interference at midlatitudes. *Midlatitude Ionospheric Dynamics and Disturbances, Geophys. Monogr. Ser*, *181*, 291–295. doi: 10.1029/181GM26

Mishin, E., Nishimura, Y., & Foster, J. (2017). Saps/said revisited: A causal relation to the substorm current wedge. *Journal of Geophysical Research: Space Physics*, *122*(8), 8516–8535. doi: 10.1002/2017JA024263

Moffett, R., & Quegan, S. (1983). The mid-latitude trough in the electron concentration of the ionospheric f-layer: a review of observations and modelling. *Journal of Atmospheric and Terrestrial Physics*, *45*(5), 315–343. doi: 10.1016/S0021-9169(83)80038-5

Newell, P., Sotirelis, T., & Wing, S. (2009). Diffuse, monoenergetic, and broadband aurora: The global precipitation budget. *Journal of Geophysical Research: Space Physics*, *114*(A9). doi: 10.1029/2009JA014326

Ohtani, S. (2021). Revisiting the partial ring current model: Longitudinal asymmetry of ground magnetic depression during geomagnetic storms. *Journal of Geophysical Research: Space Physics*, e2021JA029643. doi: 10.1029/2021JA029643

Ohtani, S., Gjerloev, J., Anderson, B., Kataoka, R., Troshichev, O., & Watari, S. (2018). Dawnside wedge current system formed during intense geomagnetic storms. *Journal of Geophysical Research: Space Physics*, *123*(11), 9093–9109. doi: 10.1029/2018JA025678

Pham, K., Zhang, B., Sorathia, K., Dang, T., Wang, W., Merkin, V., ... others (2022). Thermospheric density perturbations produced by traveling atmospheric disturbances during august 2005 storm. *Journal of Geophysical Research: Space Physics*, *127*(2), e2021JA030071. doi: 10.1029/2021JA030071

Richmond, A., Ridley, E., & Roble, R. (1992). A thermosphere/ionosphere general circulation model with coupled electrodynamics. *Geophysical Research Letters*, *19*(6), 601–604. doi: 10.1029/92GL00401

Rodger, A., Moffett, R., & Quegan, S. (1992). The role of ion drift in the formation of ionisation troughs in the mid-and high-latitude ionosphere—a review. *Journal of Atmospheric and Terrestrial Physics*, *54*(1), 1–30. doi: 10.1016/0021-9169(92)90082-V

Shepherd, S., & Ruohoniemi, J. (2000). Electrostatic potential patterns in the high-latitude ionosphere constrained by superdarn measurements. *Journal of Geophysical Research: Space Physics*, *105*(A10), 23005–23014. doi: 10.1029/2000JA000171

Sorathia, K., Merkin, V., Panov, E., Zhang, B., Lyon, J., Garretson, J., ... Wiltberger, M. (2020). Ballooning-interchange instability in the near-earth plasma sheet and auroral beads: Global magnetospheric modeling at the limit of the mhd approximation. *Geophysical research letters*, *47*(14), e2020GL088227. doi: 10.1029/2020GL088227

Sorathia, K., Merkin, V., Ukhorskiy, A., Mauk, B., & Sibeck, D. (2017). Energetic particle loss through the magnetopause: A combined global mhd and test-particle study. *Journal of Geophysical Research: Space Physics*, *122*(9), 9329–9343. doi: 10.1002/2017JA024268

Sorathia, K., Michael, A., Merkin, V. G., Ukhorskiy, A. Y., Turner, D. L., Lyon, J., ... Toffoletto, F. (2021). The role of mesoscale plasma sheet dynamics in ring current formation. *Frontiers in Astronomy and Space Sciences*, 192. doi: 10.3389/fspas.2021.761875

Sorathia, K. A., Ukhorskiy, A. Y., Merkin, V. G., Fennell, J. F., & Claudepierre, S. G. (2018). Modeling the depletion and recovery of the outer radiation belt during a geomagnetic storm: Combined mhd and test particle simulations. *Journal of Geophysical Research: Space Physics*, *123*(7), 5590–5609. doi: 10.1029/2018JA025506

Spiro, R., Heelis, R., & Hanson, W. (1978). Ion convection and the formation of the mid-latitude f region ionization trough. *Journal of Geophysical Research: Space Physics*, *83*(A9), 4255–4264. doi: 10.1029/JA083iA09p04255

Toffoletto, F., Sazykin, S., Spiro, R., & Wolf, R. (2003). Inner magnetospheric modeling with the rice convection model. *Space Science Reviews*, *107*(1-2), 175–196. doi: 10.1023/A:1025532008047

Ukhorskiy, A. Y., Sitnov, M. I., Millan, R. M., Kress, B. T., Fennell, J., Claudepierre, S., & Barnes, R. (2015). Global storm time depletion of the outer electron belt. *Journal of Geophysical Research: Space Physics*, *120*(4), 2543–2556. doi: 10.1002/2014JA020645

Vasyliunas, V. M. (1970). Mathematical models of magnetospheric convection and its coupling to the ionosphere. In *Particles and fields in the magnetosphere* (pp. 60–71). Springer. doi: 10.1007/978-94-010-3284-1_6

Voiculescu, M., & Roth, M. (2008). Eastward sub-auroral ion drifts or asaid. In *Annales geophysicae* (Vol. 26, pp. 1955–1963). doi: 10.5194/angeo-26-1955-2008

Wang, W., Talaat, E. R., Burns, A. G., Emery, B., Hsieh, S.-y., Lei, J., & Xu, J. (2012). Thermosphere and ionosphere response to subauroral polarization streams (saps): Model simulations. *Journal of Geophysical Research: Space Physics*, *117*(A7). doi: 10.1029/2012JA017656

Wolf, R. (1983). The quasi-static (slow-flow) region of the magnetosphere. In *Solar-terrestrial physics* (pp. 303–368). Springer. doi: 10.1007/978-94-009-7194-3_14

Xiong, C., Lühr, H., Wang, H., & Johnsen, M. G. (2014). Determining the boundaries of the auroral oval from champ field-aligned current signatures–part 1. In *Annales geophysicae* (Vol. 32, pp. 609–622). doi: 10.5194/angeo-32-609-2014

Zhang, B., Sorathia, K. A., Lyon, J. G., Merkin, V. G., Garretson, J. S., & Wiltberger, M. (2019). Gamera: A three-dimensional finite-volume mhd solver for non-orthogonal curvilinear geometries. *The Astrophysical Journal Supplement Series*, *244*(1), 20. doi: 10.3847/1538-4365/ab3a4c

Zhang, B., Sorathia, K. A., Lyon, J. G., Merkin, V. G., & Wiltberger, M. (2019b). Conservative averaging-reconstruction techniques (ring average) for 3-d finite-volume mhd solvers with axis singularity. *Journal of Computational Physics*, *376*, 276–294. doi: 10.1016/j.jcp.2018.08.020

Zhang, J., Dere, K., Howard, R., & Bothmer, V. (2003). Identification of solar sources of major geomagnetic storms between 1996 and 2000. *The Astrophysical Journal*, *582*(1), 520. doi: 10.1086/344611

Zhao, H., Li, X., Baker, D., Fennell, J., Blake, J., Larsen, B. A., ... others (2015). The evolution of ring current ion energy density and energy content during geomagnetic storms based on van allen probes measurements. *Journal of Geophysical Research: Space Physics*, *120*(9), 7493–7511. doi: 10.1002/2015JA021533

Zheng, Y., Lui, A., Fok, M.-C., Anderson, B., Brandt, P., Immel, T., & Mitchell, D. (2006). Relationship between region 2 field-aligned current and the ring current: Model results. *Journal of Geophysical Research: Space Physics*, *111*(A11). doi: 10.1029/2006JA011603

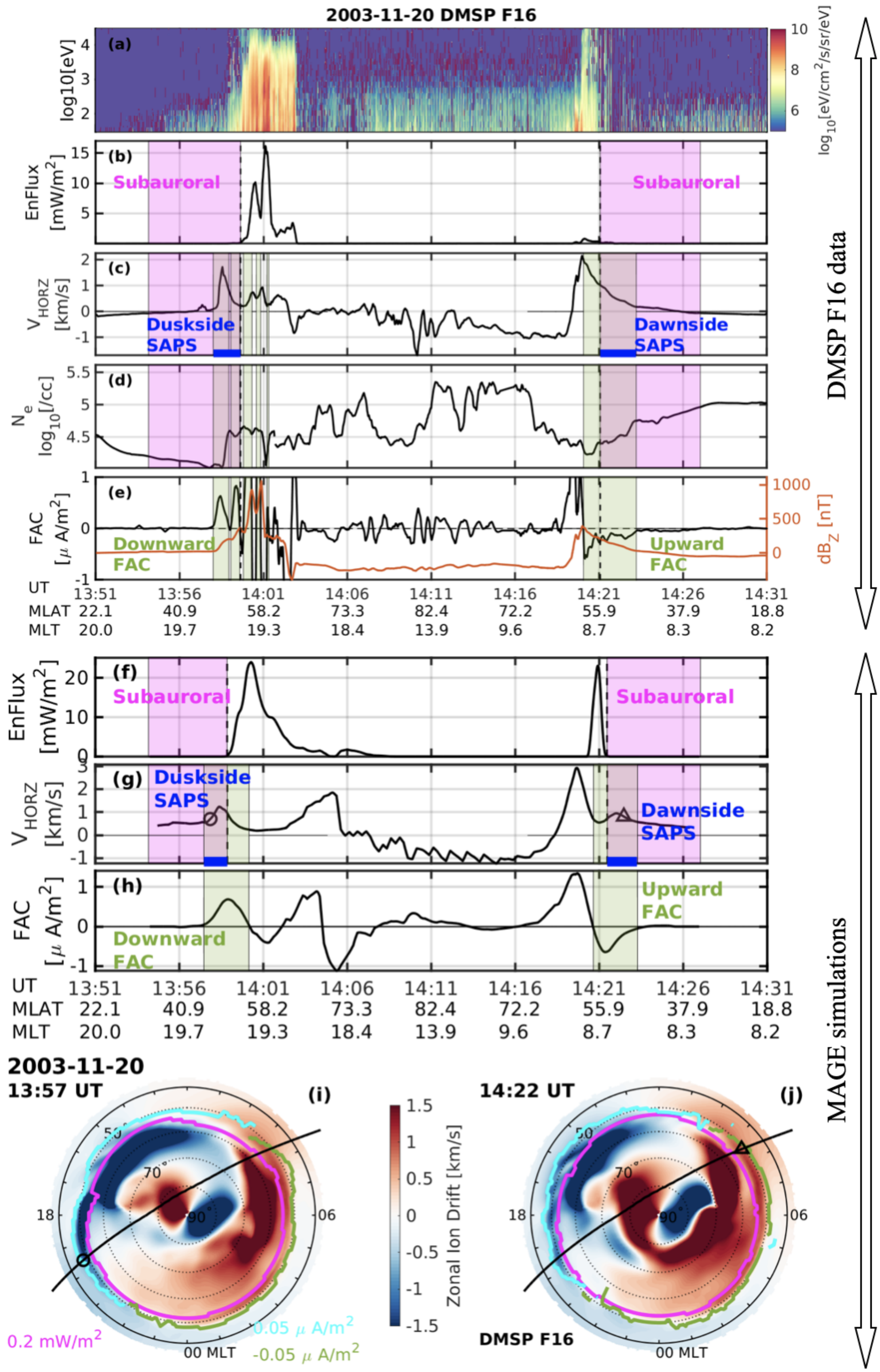

Figure 2. (a-e) SAPS observed by DMSP F16 and (f-j) simulated by the MAGE model from 13:51 UT to 14:31 UT. (a) Electron precipitation energy spectrum. (b) Integrated electron precipitation energy flux ($EnFlux$). (c) Cross track ion drift velocity (V_{HORZ}). (d) Electron density. (e) Cross-track horizontal magnetic perturbation (orange) and the derived FAC density (black).

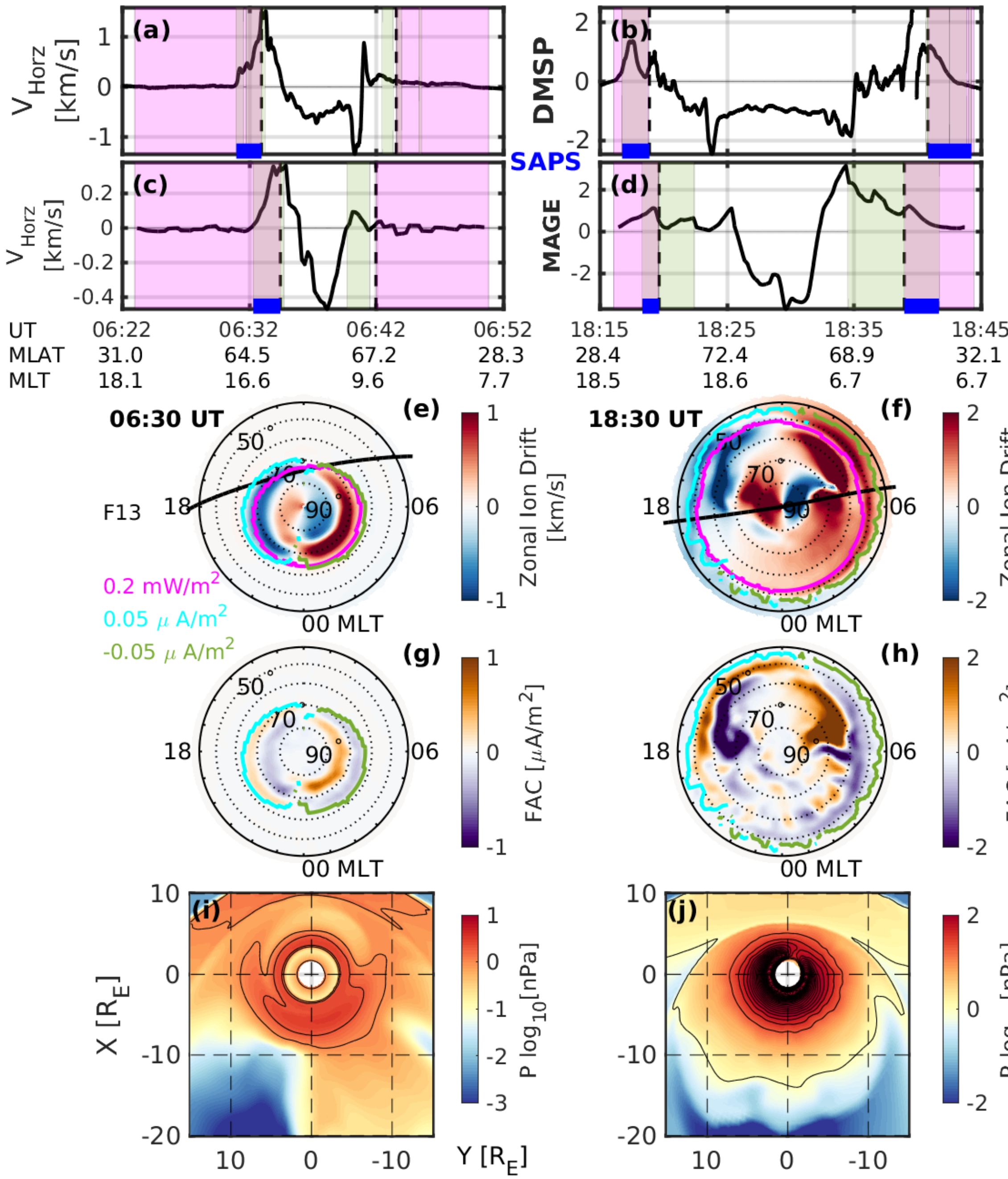

Figure 3. Comparison of SAPS between storm time and before the storm. (a-b) DMSP F13 measurements of V_{HORZ} during 06:22-06:52 UT, and during 18:15-18:45 UT. (c-d) MAGE simulation results of V_{HORZ} sampled along DMSP F13 trajectories during the two intervals. (e-h) MAGE simulation results of zonal ion drift and FAC in the northern hemispheric ionosphere at 06:30 UT and 18:30 UT, respectively. (i-j) Plasma pressure distribution in the magnetospheric equatorial plane at 06:30 UT and 18:30 UT on a logarithmic scale.

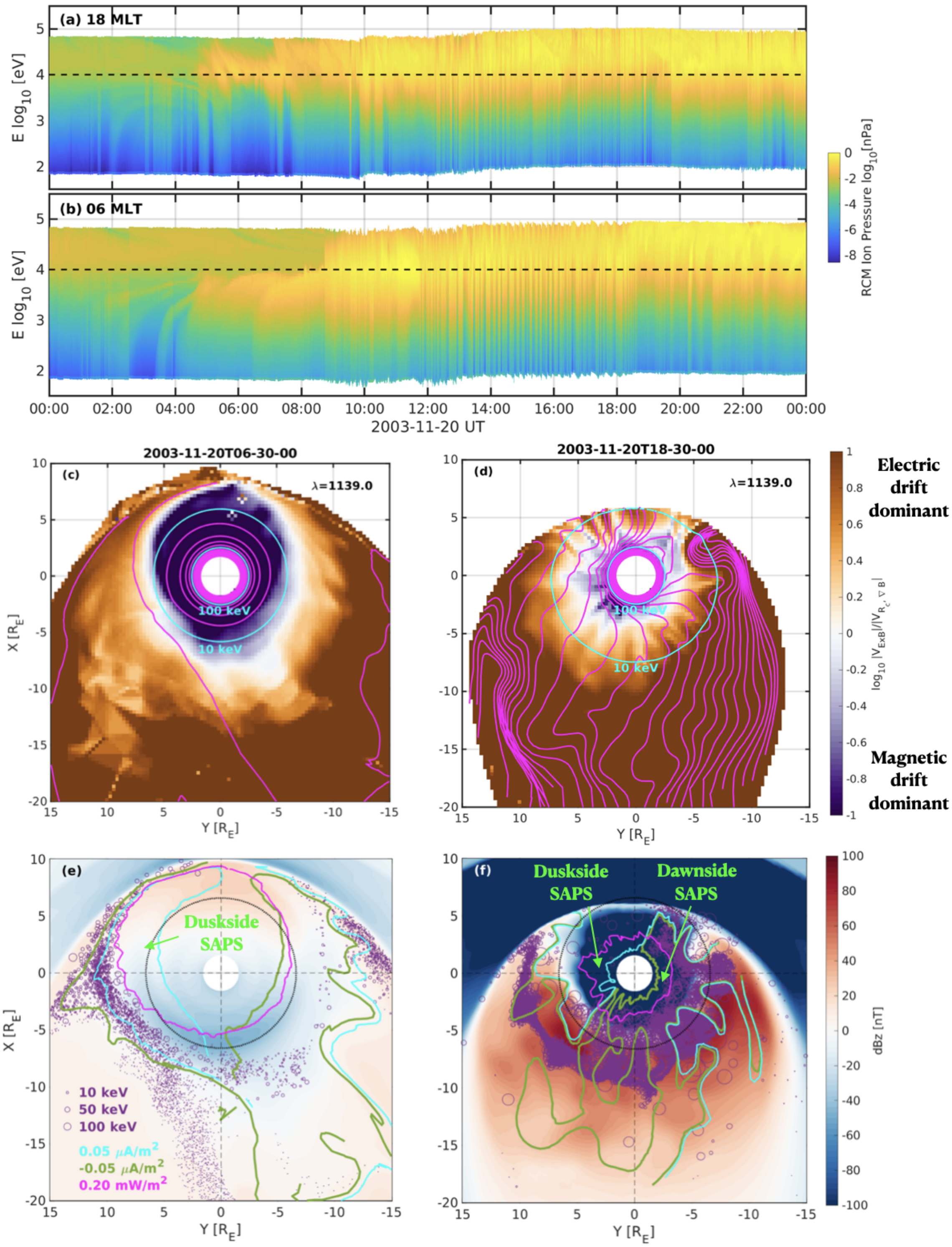

Figure 4. (a-b) Ring current pressure sampled at the geosynchronous orbit at 18 MLT and 06 MLT. (c-d) Ratio between electrostatic drift and magnetic drift speeds of ions with the same energy invariant. The cyan curves show contours of kinetic energy of 10 keV and 100 keV. The magenta curves show contours of effective potential separated by 20 kV, equivalent to ion drift path. (e-f) Equatorial distributions of test particle protons 30 minutes after they were released at 06 UT and 18 UT. The colorbar shows residual magnetic field B_Z with dipole background subtracted. The green, cyan, and magenta curves are ionospheric boundaries of upward and downward FACs, and equatorward boundary of electron precipitation, respectively, mapped from the northern hemisphere along geomagnetic field lines.

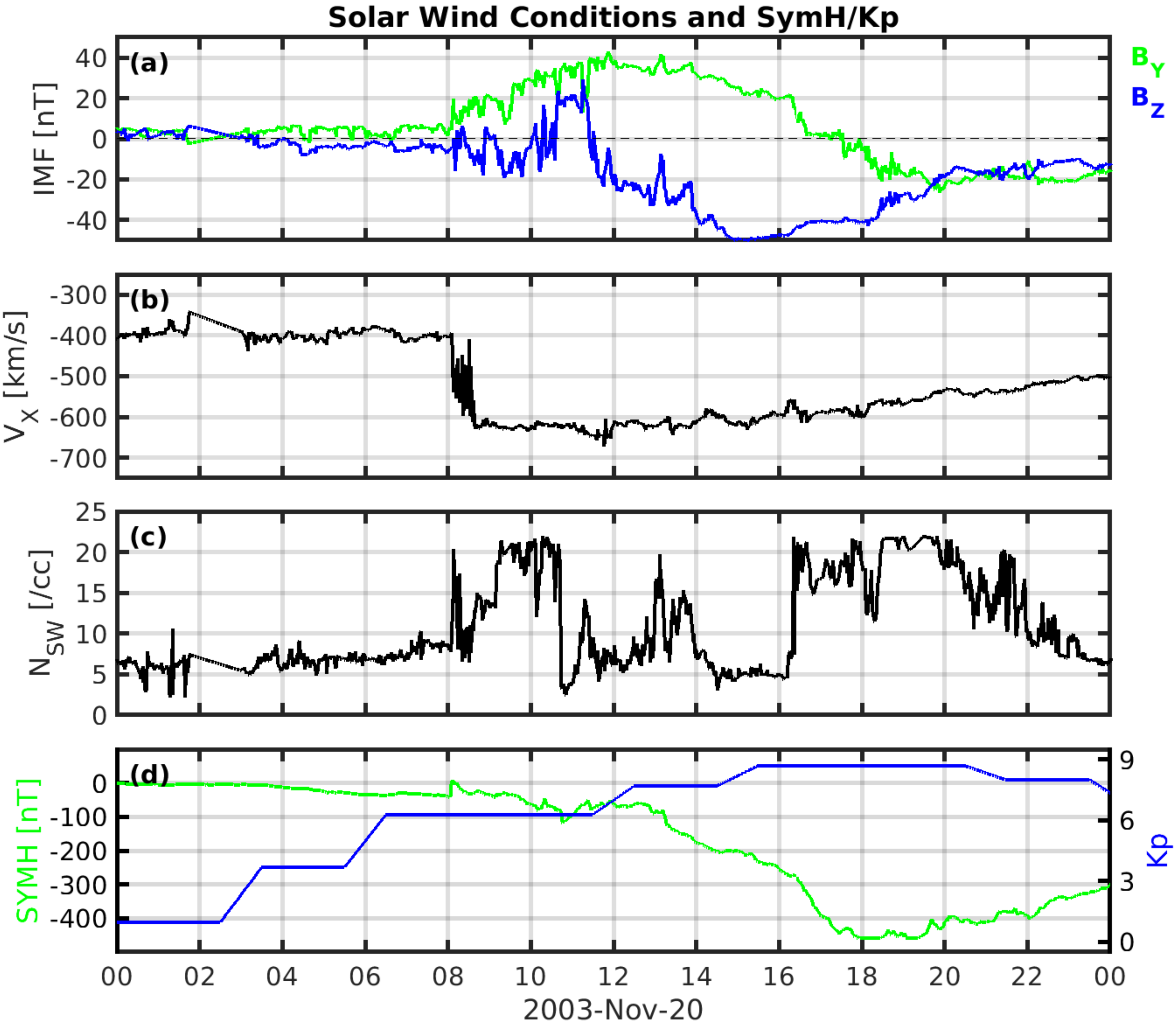

Solar Wind Conditions and SymH/Kp
(a)
IMF [nT]
40
20
0
-20
-40
B_Y
B_Z
(b)
V_X [km/s]
-300
-400
-500
-600
-700
(c)
N_{SW} [/cc]
25
20
15
10
5
0
(d)
SYMH [nT]
0
-100
-200
-300
-400
Kp
9
6
3
0
00
02
04
06
08
10
12
14
16
18
20
22
00
2003-Nov-20

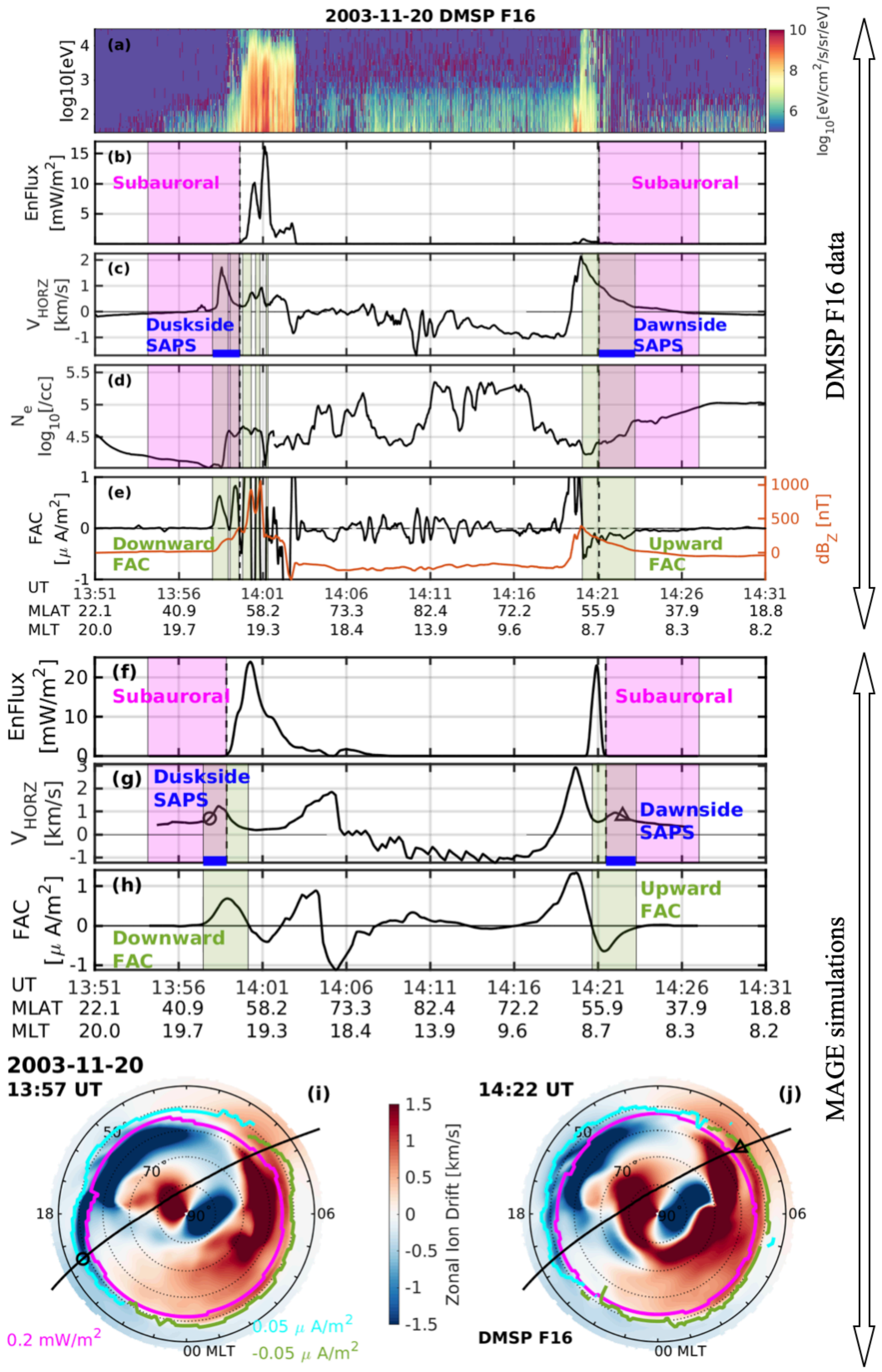
2003-11-20 DMSP F16
(a)
log10[eV]
log$_{10}$[eV/cm^2/s/sr/eV]
(b)
EnFlux [mW/m^2]
Subauroral
Subauroral
(c)
V$_{HORZ}$ [km/s]
Duskside SAPS
Dawnside SAPS
(d)
N$_e$ log$_{10}$[/cc]
(e)
FAC [μ A/m^2]
Downward FAC
Upward FAC
dB$_Z$ [nT]
UT 13:51 13:56 14:01 14:06 14:11 14:16 14:21 14:26 14:31
MLAT 22.1 40.9 58.2 73.3 82.4 72.2 55.9 37.9 18.8
MLT 20.0 19.7 19.3 18.4 13.9 9.6 8.7 8.3 8.2
DMSP F16 data
(f)
EnFlux [mW/m^2]
Subauroral
Subauroral
(g)
V$_{HORZ}$ [km/s]
Duskside SAPS
Dawnside SAPS
(h)
FAC [μ A/m^2]
Upward FAC
Downward FAC
UT 13:51 13:56 14:01 14:06 14:11 14:16 14:21 14:26 14:31
MLAT 22.1 40.9 58.2 73.3 82.4 72.2 55.9 37.9 18.8
MLT 20.0 19.7 19.3 18.4 13.9 9.6 8.7 8.3 8.2
MAGE simulations
2003-11-20
13:57 UT
(i)
14:22 UT
(j)
Zonal Ion Drift [km/s]
0.2 mW/m^2
0.05 μ A/m^2
-0.05 μ A/m^2
00 MLT
18
06
DMSP F16
00 MLT

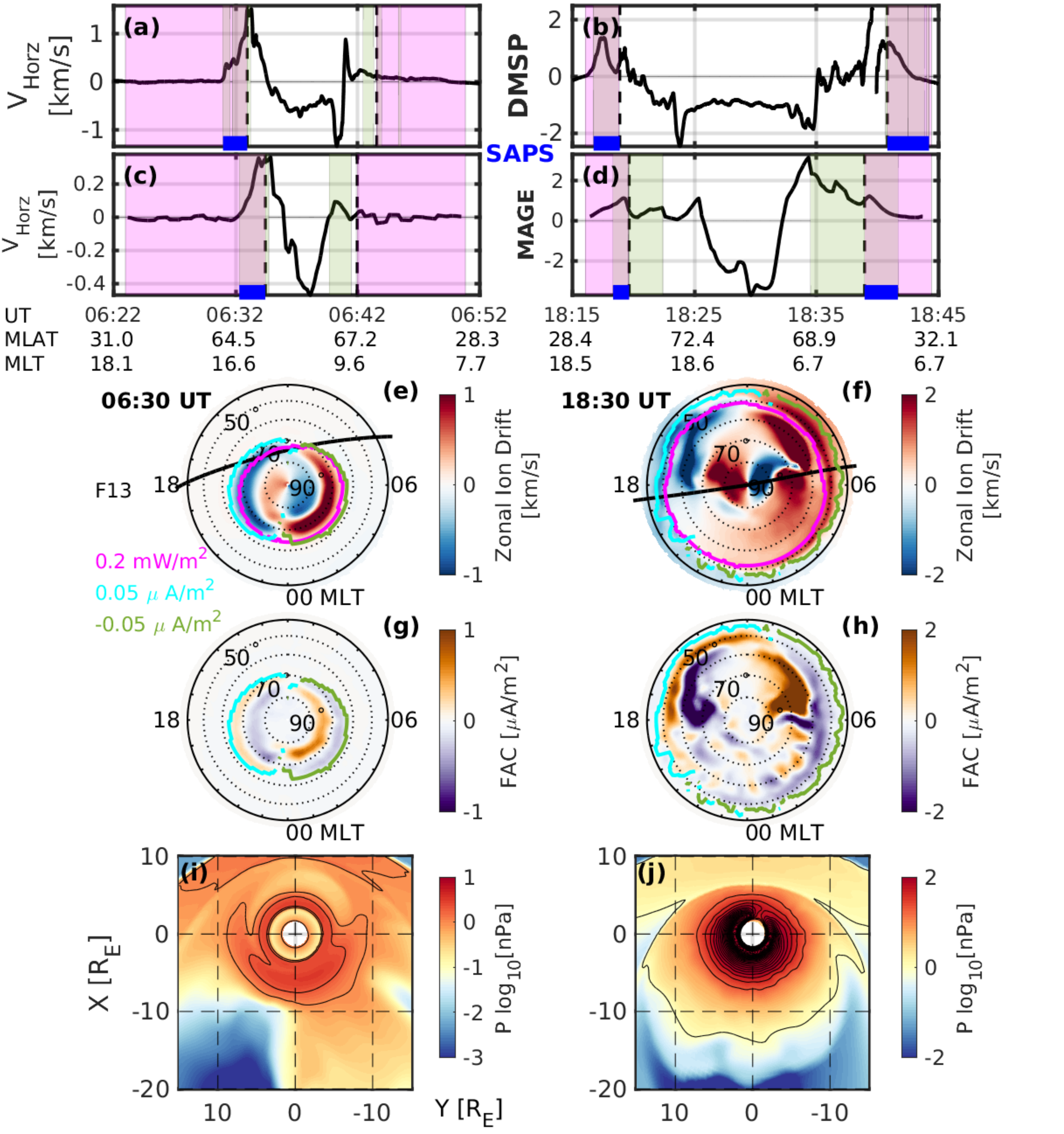

(a)
(b)
(c)
(d)
V_Horz [km/s]
DMSP
SAPS
MAGE
UT 06:22 06:32 06:42 06:52 18:15 18:25 18:35 18:45
MLAT 31.0 64.5 67.2 28.3 28.4 72.4 68.9 32.1
MLT 18.1 16.6 9.6 7.7 18.5 18.6 6.7 6.7
06:30 UT
(e)
18:30 UT
(f)
F13
Zonal Ion Drift [km/s]
0.2 mW/m^2
0.05 μ A/m^2
-0.05 μ A/m^2
00 MLT
18
06
(g)
(h)
FAC [μA/m^2]
(i)
(j)
X [R_E]
Y [R_E]
P log_10[nPa]

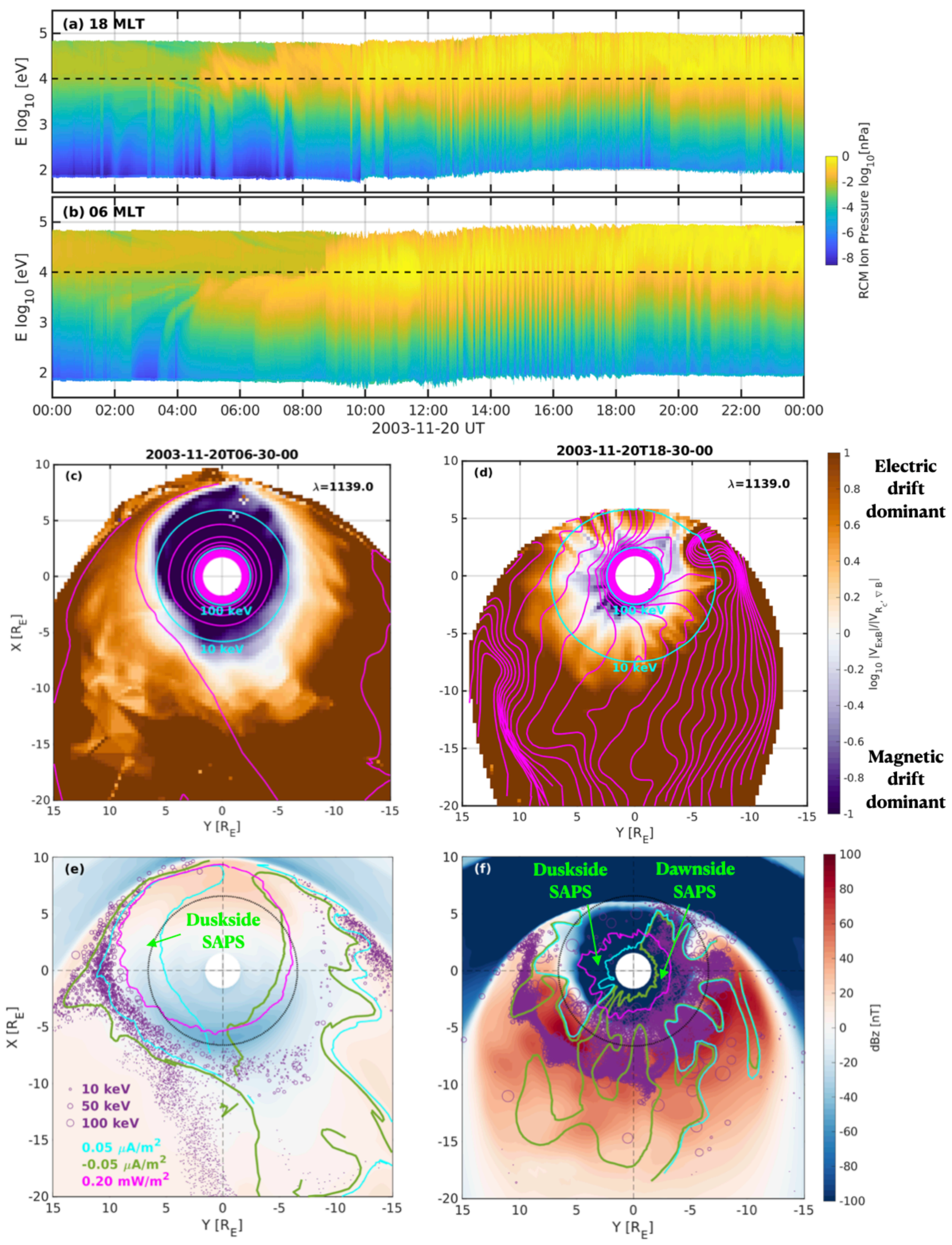

(a) 18 MLT
(b) 06 MLT
E log10 [eV]
RCM Ion Pressure log10[nPa]
2003-11-20 UT
00:00
02:00
04:00
06:00
08:00
10:00
12:00
14:00
16:00
18:00
20:00
22:00
00:00
2003-11-20T06-30-00
2003-11-20T18-30-00
(c)
(d)
λ=1139.0
100 keV
10 keV
X [RE]
Y [RE]
Electric drift dominant
Magnetic drift dominant
log10 |VExB|/|VRc, ∇B|
(e)
(f)
Duskside SAPS
Dawnside SAPS
10 keV
50 keV
100 keV
0.05 μA/m2
-0.05 μA/m2
0.20 mW/m2
dBz [nT]

AGU PUBLICATIONS

AGU Advance

Supporting Information for

Ionospheric Dawnside Subauroral Polarization Streams: A Unique Feature of Major Geomagnetic Storms

Dong Lin[1], Wenbin Wang[1], Viacheslav Merkin[2], Chaosong Huang[3], Meers Oppenheim[4], Kareem Sorathia[2], Kevin Pham[1], Adam Michael[2], Shanshan Bao[5], Qian Wu[1], Yongliang Zhang[2], Michael Wiltberger[1], Frank Toffoletto[5], John Lyon[6], and Jeffrey Garretson[2].

[1]High Altitude Observatory, National Center for Atmospheric Research, Boulder CO,
[2]Applied Physics Laboratory, Johns Hopkins University, Laurel MD,
[3]Space Vehicles Directorate, Air Force Research Laboratory, Kirtland AFB, NM,
[4]Department of Astronomy, Boston University, Boston MA,
[5]Department of Physics and Astronomy, Rice University, Houston TX,
[6]Department of Physics and Astronomy, Dartmouth College, Hanover NH

Contents of this file

Figures S1-S11.
Caption for Movie S1 and S2.

Introduction

This supporting information provides additional figures of dawnside and duskside SAPS observed by DMSP (Figures S1-S5), simulated by MAGE (Figures S6-S7), comparison of electric and magnetic drifts (Figure S8), energetic proton fluxes measured by the LANL satellites at the geosynchronous orbit (Figure S9), controlled MAGE simulation experiments with ten times reduced IMF (Figure S10) and zero IMF B_Y (Figure S11), and animations showing the test particle convection-drift in the magnetosphere obtained with the CHIMP test particle simulations.

Figure S1. Dawnside and duskside SAPS observed by DMSP F13 from 14:02 UT to 14:32 UT. The format is similar to that in Figure 2 of the main manuscript.

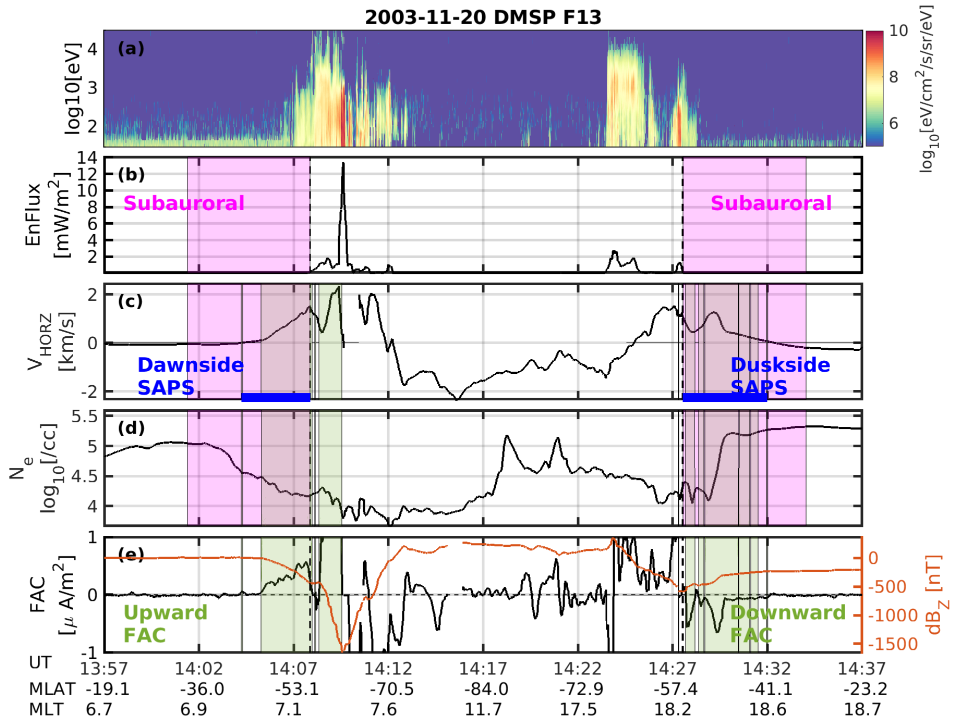

Figure S2. Dawnside and duskside SAPS observed by DMSP F14 from 14:09 UT to 14:49 UT. The format is similar to that in Figure 2 of the main manuscript.

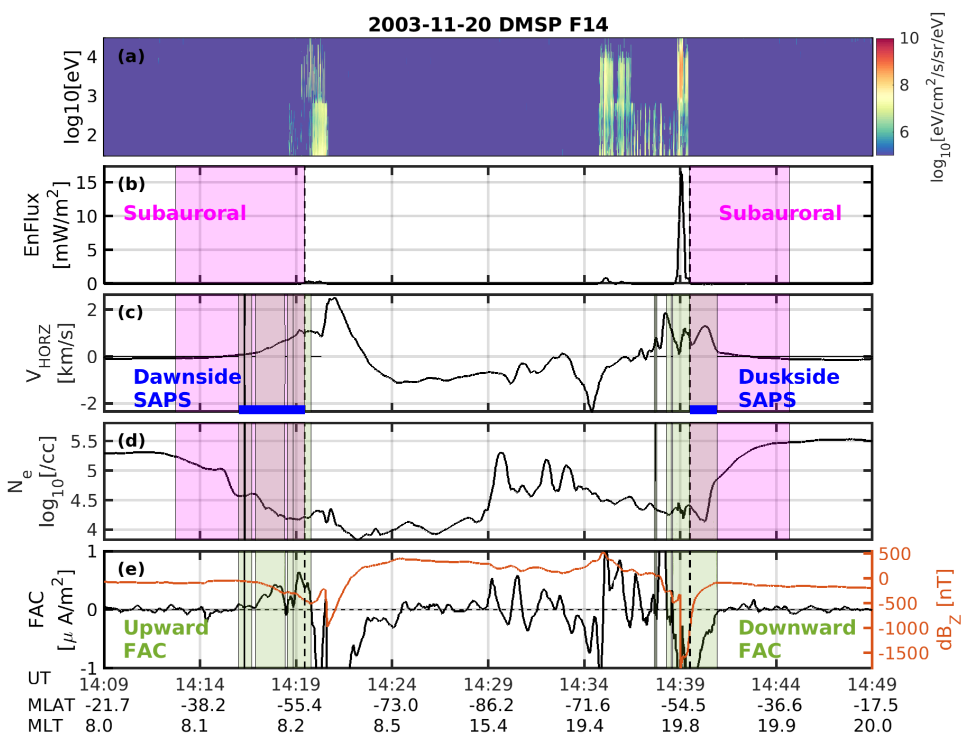

Figure S3. Duskside SAPS observed by DMSP F15 from 13:40 UT to 14:20 UT. No substantial dawnside SAPS are identified. It is probably because the auroral crossing point of 11 MLT was near the eastward end of the dawnside SAPS channel. The format is similar to that in Figure 2 of the main manuscript.

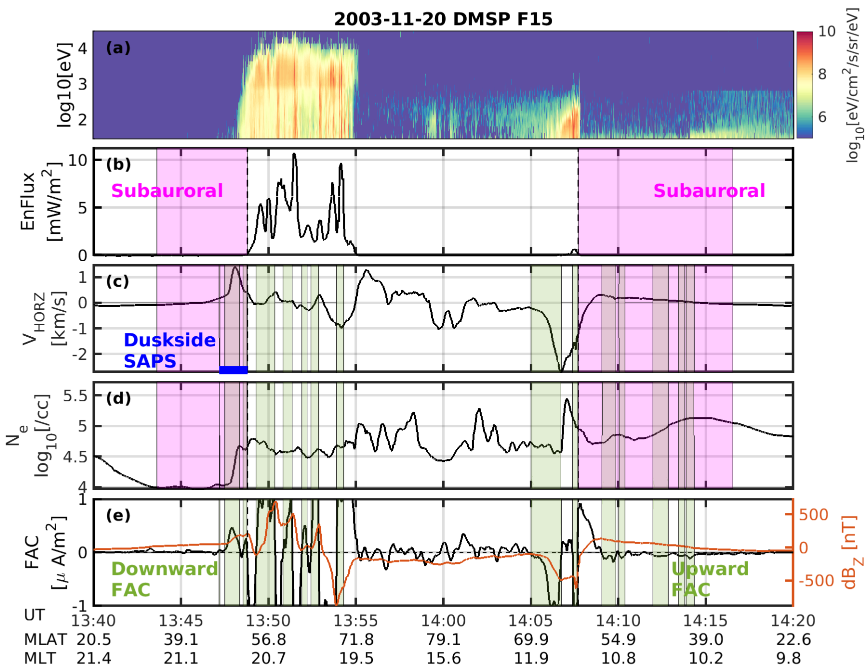

Figure S4. Duskside SAPS observed by DMSP F13 during 06:17-06:57 UT. This plot contains more detailed information than Figure 3a in the main manuscript, where only the horizontal ion drift and auroral and FAC boundaries are shown.

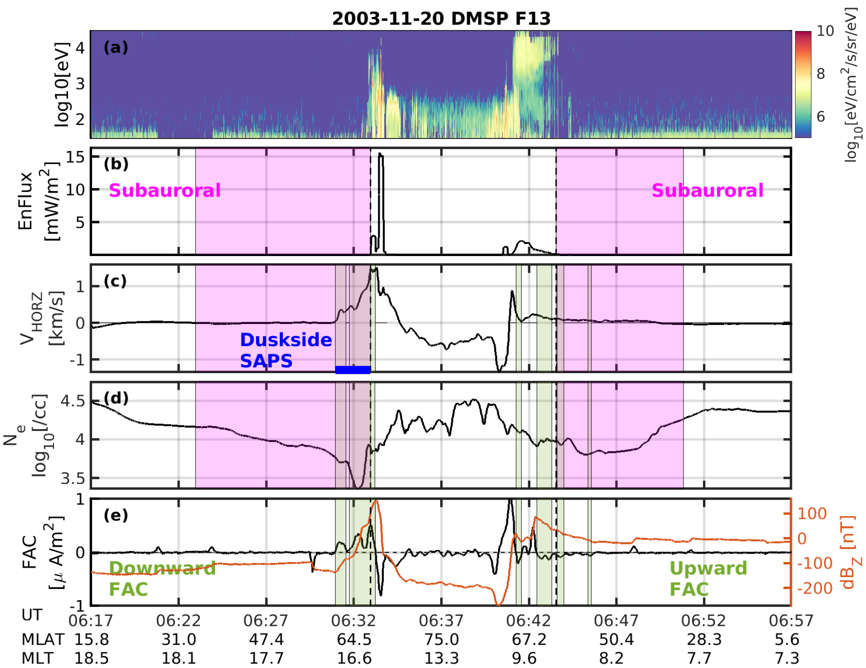

Figure S5. Duskside and dawnside SAPS observed by DMSP F13 during 18:10-18:50 UT. This plot contains more detailed information than Figure 3b in the main manuscript, where only the horizontal ion drift and auroral and FAC boundaries are shown.

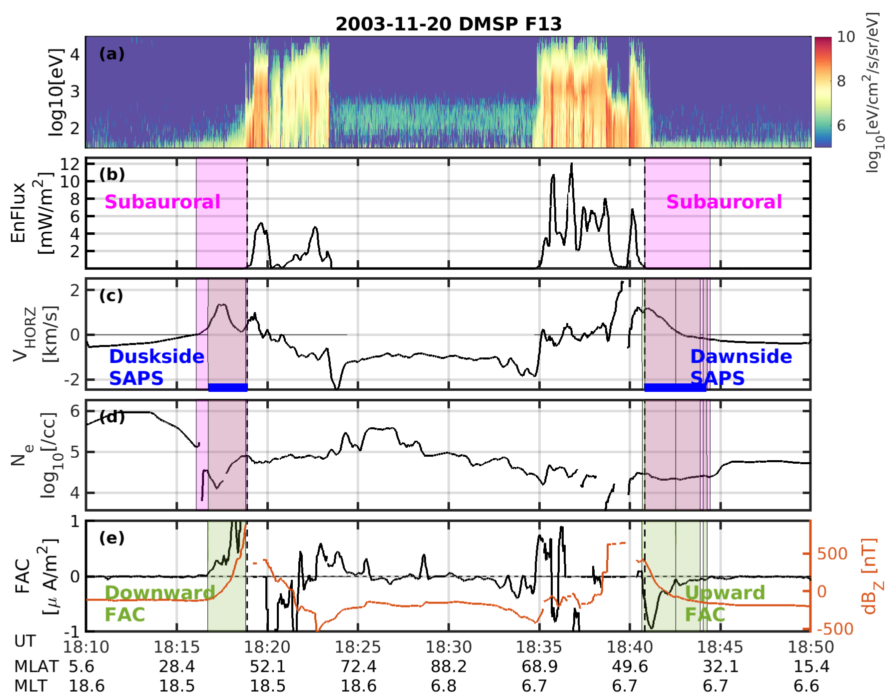

Figure S6. Duskside SAPS simulated by MAGE during 06:17-06:57 UT. This plot contains more detailed information than Figure 3c in the main manuscript, where only the horizontal ion drift and auroral and FAC boundaries are shown.

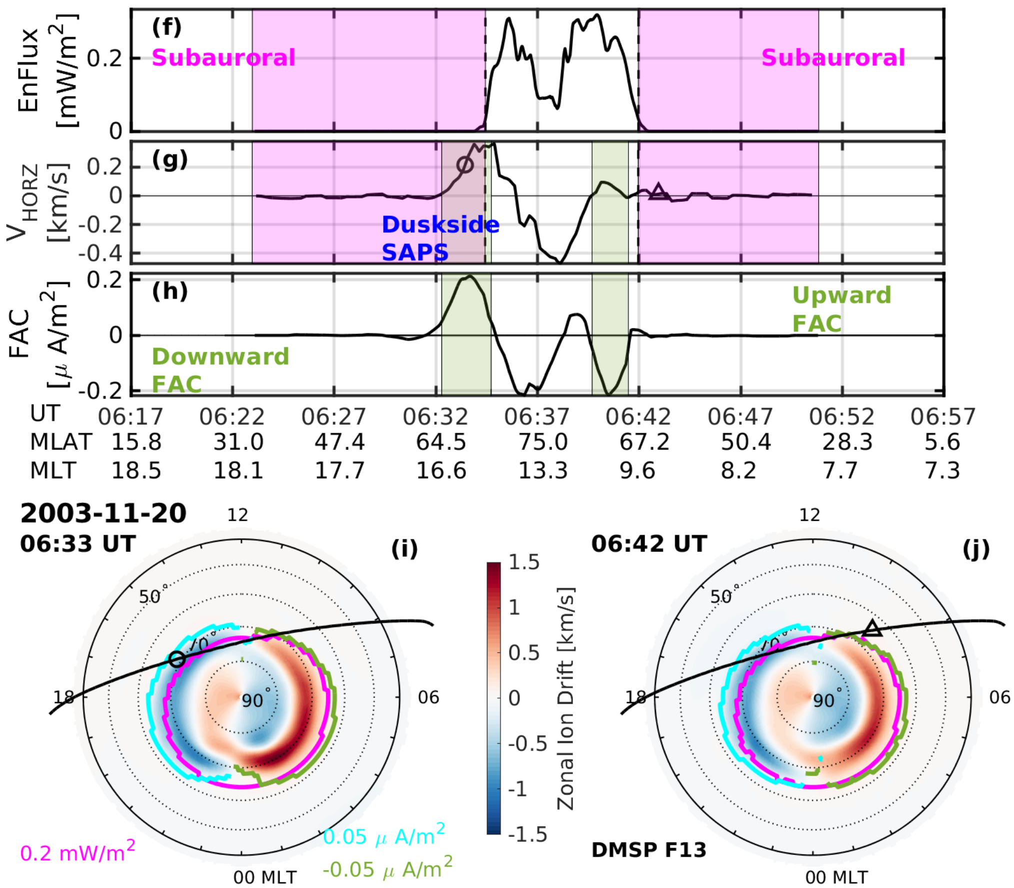

Figure S7. Duskside and dawnside SAPS simulated by MAGE during 18:10-18:50 UT. This plot contains more detailed information than Figure 3d in the main manuscript, where only the horizontal ion drift and auroral and FAC boundaries are shown.

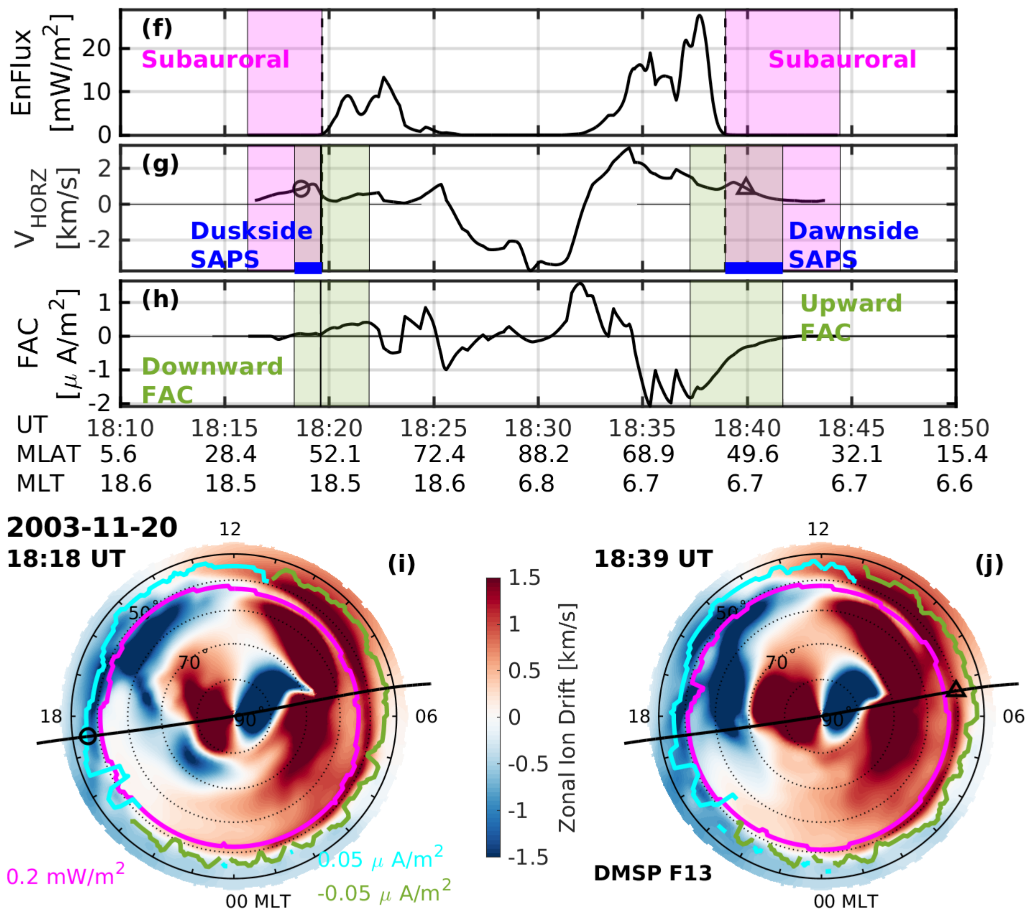

Figure S8. Ratio between electric and magnetic drifts for additional two energy invariants at 06:30 UT and 18:30 UT. Similar to the comparison shown in Figures 4c-4d based on lambda=1139.0, the ions with lambda=338.2 and lambda=3032.9 are also dominated by magnetic drifts at 06:30 UT and by electric drifts at 18:30 UT when they are energized to 10-100 keV during the adiabatic inward transport.

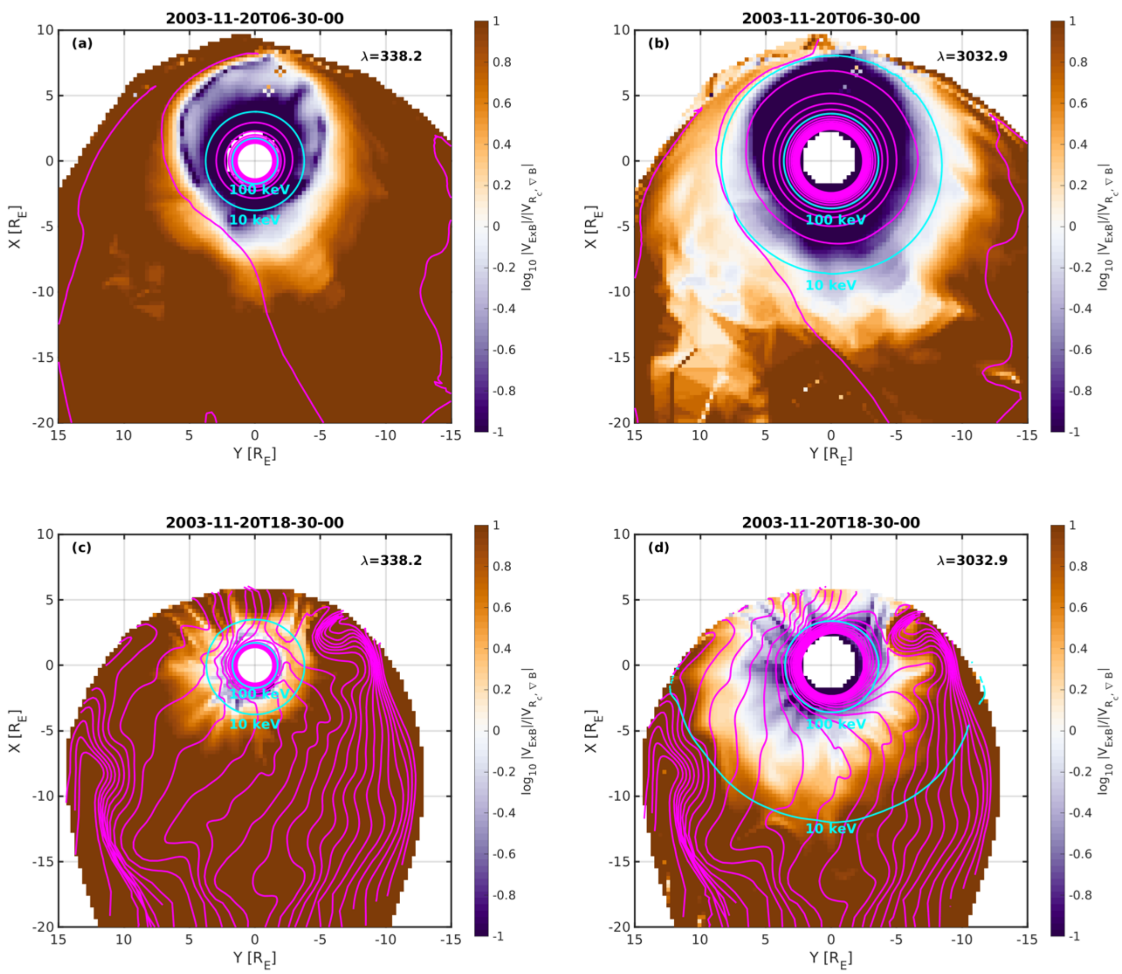

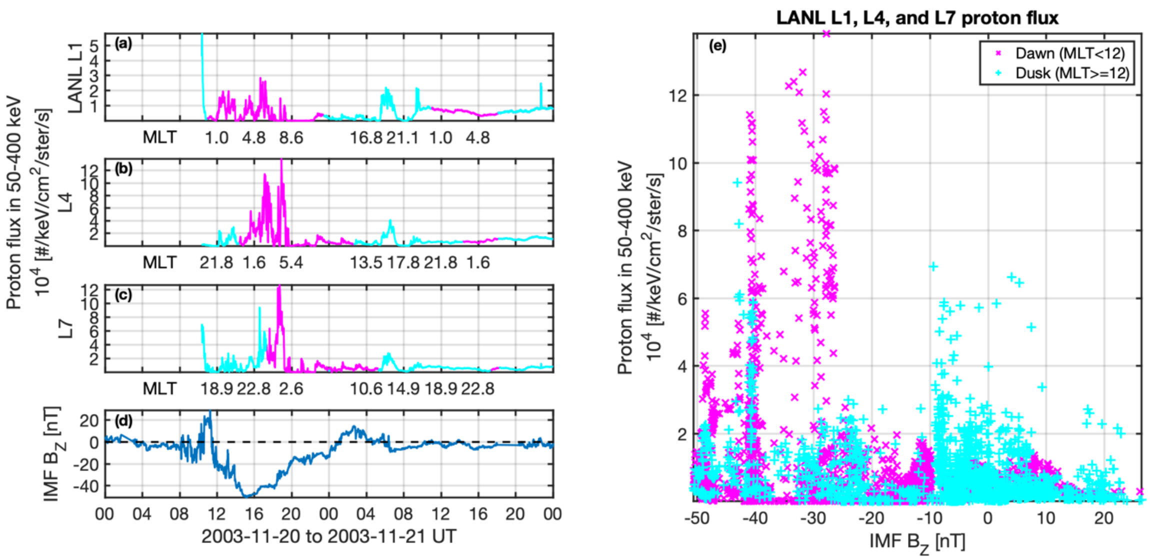

Figure S9. (a-c) Energetic proton fluxes in the energy range of 50-400 keV measured by the LANL L1, L4, and L7 satellites during 20-21 November 2003. The LANL satellites were in a geosynchronous orbit at different MLTs. The magenta curves indicate when each satellite was in the dawn sector, i.e., MLT<12. The cyan curves indicate when the satellites were in the dusk sector, i.e., MLT>=12. (d) IMF B_Z. (e) Energetic proton flux distribution with IMF B_Z when the satellites were in dawn (magenta crosses) and in the dusk (cyan pluses).

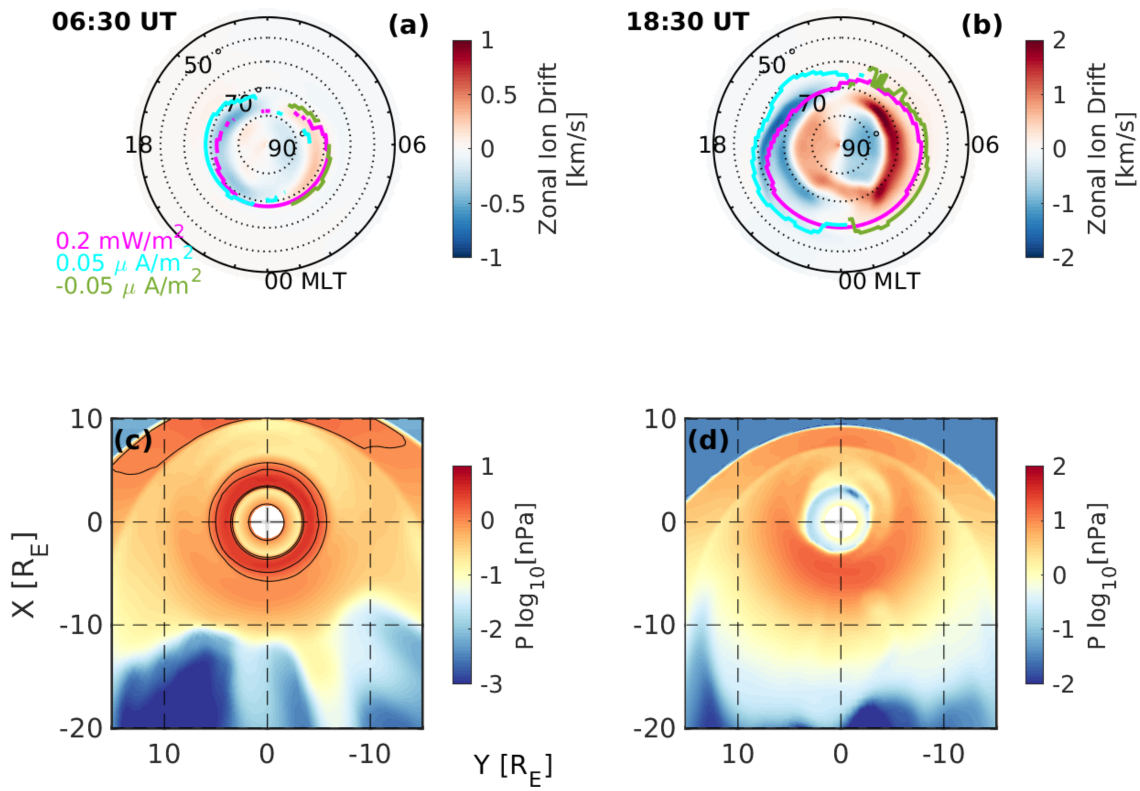

Figure S10. Controlled simulation results with ten times reduced IMF. (a-b) Zonal ion drifts in the northern hemisphere ionosphere with a similar format to Figures 3e-3f. (c-d) Plasma pressure in the magnetospheric equatorial plane with a similar format to Figures 3g-3h. Both before the storm commencement at 06:30 UT and during the main phase at 18:30 UT, duskside SAPS are formed in the gap between the equatorward boundary of electron precipitation (magenta curves around 18 MLT) and the equatorward boundary of downward Region-2 FACs (cyan curves around 18 MLT). But there are no obvious dawnside SAPS even during the main phase when the IMF is reduced by ten times. The sawtooth like upward FAC boundary in the prenoon sector at 18:30 UT in panel (b) is due to small scale FAC structures at ~50 deg MLAT.

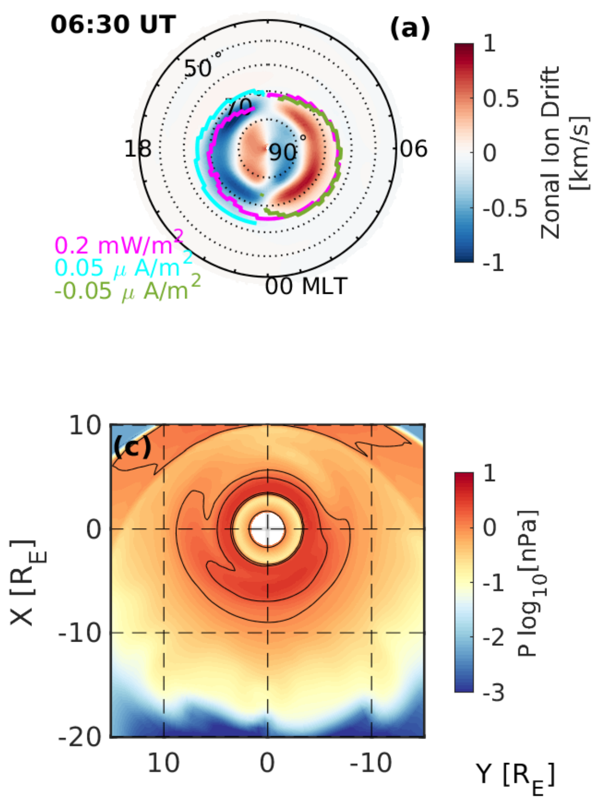

Figure S11. Controlled simulation results with IMF B_Y=0. (a-b) Zonal ion drifts in the northern hemisphere ionosphere with a similar format to Figures 3e-3f. (c-d) Plasma pressure in the magnetospheric equatorial plane with a similar format to Figures 3g-3h. Both before the storm commencement at 06:30 UT and during the main phase at 18:30 UT, duskside SAPS are formed in the gap between the equatorward boundary of electron precipitation (magenta curves around 18 MLT) and the equatorward boundary of downward Region-2 FACs (cyan curves around 18 MLT). Substantial dawnside SAPS are still formed during the main phase despite zero IMF B_Y.

Movie S1. A movie showing the evolution of test particles released from the nightside plasma sheet at 06 UT. The format is similar to that in Figure 4c and 4d in the main manuscript. The purple circles indicate the energy of the protons. The background is the residual magnetic field, i.e., Bz subtracted by the dipole magnetic field. The green and cyan curves are upward and downward ionospheric FAC boundaries defined with a threshold of 0.05 microA/m^2 and mapped from the northern hemisphere ionosphere along geomagnetic field lines to the equatorial plane. Plots of similar format are combined in Movie S1. The mapping of FAC boundaries is shown every ten minutes.

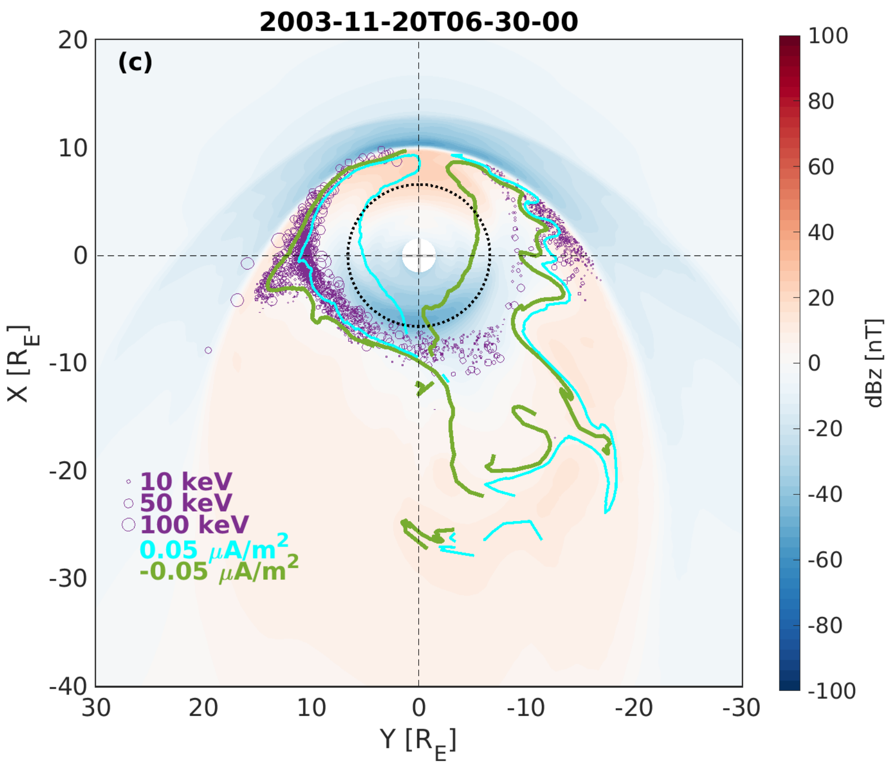

Movie S2. Similar format to Movie S1. The particles are released from 18UT.